ELSEVIER

Contents lists available at ScienceDirect

Journal of Inorganic Biochemistry

journal homepage: www.elsevier.com/locate/jinorgbio



The cytochrome P450 decarboxylase from *Staphylococcus aureus* can produce a diene from a C18 monounsaturated fatty acid: A spectroscopic, structural and kinetic characterisation

Lewis J. Williams ^{a,b}, Michael T. Wilson ^a, James A. Birrell ^a, Harry W. Lang ^a, Stephen G. Bell ^c, Jonathan A.R. Worrall ^{a,*}

- ^a School of Life Sciences, University of Essex, Wivenhoe Park, Colchester CO4 3SQ, UK
- ^b Diamond Light Source, Harwell Science and Innovation Campus, Didcot OX11 0DE, UK
- ^c Department of Chemistry, University of Adelaide, Adelaide, SA 5005, Australia

ARTICLE INFO

Keywords: Peroxygenase Unsaturated fatty acid Decarboxylase Diene X-ray crystallography Ferryl heme

ABSTRACT

Certain members of the bacterial cytochrome P450 152 family (CYP152) are peroxygenases that catalyse the decarboxylation of fatty acids into terminal olefins making them attractive biocatalysts for biofuel production. To date, the characterisation of decarboxylating CYP152s has mainly focused on their reaction with saturated fatty acid substrates. CYP152s are often co-purified with a bound substrate, which is generally removed before further experiments are conducted. In the present work we identified that heterologous over-expressed CYP152 from Staphylococcus aureus (OleT_{Sa}) is co-purified with the trans-monounsaturated C_{18:1} fatty acid, elaidic acid. We report the spectral, thermodynamic and kinetic characteristics of OleT_{Sa} bound to both elaidic acid and its saturated counterpart, stearic acid. Despite differing spectral profiles, metabolic and kinetic studies reveal that OleT_{Sa} is capable of decarboxylating elaidic acid, converting it to heptadeca-1,8-diene following addition of hydrogen peroxide, at the same rate and chemoselectivity as the conversion of stearic acid to 1-heptadecane. The X-ray crystal structure of the as purified OleT_{Sa} in complex with elaidic acid is also presented, allowing for several key residues to be identified for site-directed mutagenesis studies. The influence of the site-directed variants on C_{18:0} and C_{18:1} product formation, binding thermodynamics and kinetics have been investigated, showing that while spectral differences occur as a likely result of perturbing the binding pocket, this does not alter the chemoselectivity of the enzyme. Our work provides important insights into the mechanism of decarboxylation of an unsaturated fatty acid substrate by OleT_{Sa} potentially expanding the sustainable substrate space available for CYP152s.

1. Introduction

Selective oxidation chemistry of inert C—H bonds is a challenging reaction for the synthetic chemist, but one that nature has overcome through the utilisation of a large ubiquitous superfamily of heme monoxygenases, cytochrome P450s (CYPs), [1] that are prevalent in many oxidative cellular processes including steroid biosynthesis, detoxification of xenobiotics and drug metabolism. [2,3] The vast majority of CYPs carry out reductive activation of molecular oxygen (O₂) to generate a

formal heme Fe(V)-oxo intermediate species, which is better described as an Fe(IV)-oxo with a delocalised radical cation within the porphyrin, referred to as Compound I. [4] This intermediate is required for H atom abstraction from the substrate to form Compound II (Fe(IV)-OH) and subsequent OH group transfer into a substrate molecule (commonly known as the oxygen rebound). [5,6] One drawback to the widespread implementation of CYPs as highly selective (stereo, regio and chemo) biocatalysts for monooxygenation reactions is the so called 'oxygen dilemma' arising from the requirement of reducing equivalents to drive

Abbreviations: CYP, cytochrome P450; ROS, reactive oxygen species; H_2O_2 , hydrogen peroxide; EPR, electron paramagnetic resonance; GC-MS, gas chromatography mass spectrometry; PDA, photodiode array; PMT, photo-multiplier tube; SVD, singular value decomposition; K_d , dissociation constant; K_{spin} , high-spin/low-spin heme equilibrium constant; WT, wild-type; Sa, Staphyloccous aureus; JE, Staphyloccous aureu

E-mail address: jworrall@essex.ac.uk (J.A.R. Worrall).

^{*} Corresponding author.

the catalytic cycle. [7] In the vast majority of CYPs, these reducing equivalents are supplied by a nicotinamide cofactor (NAD(P)H) and redox partners [8,9] that can become uncoupled from the catalytic cycle leading to futile side reactions predominately through O_2 itself acting as an electron sink, resulting in the formation of reactive oxygen species (ROS) that impair enzyme stability and function. Because of this uncoupling the reducing power supplied by an external donor can be substantially lost leading to inefficiency in turnover numbers of the CYP (i.e. moles of product formed per mole of CYP) and hydroxylation efficiency (i.e. the proportion of exogenous reducing equivalents that are productively used for substrate turnover). [7] Thus, the waste of valuable reducing equivalents and the requirement for additional enzymes for electron transfer, cofactor regeneration and to mop up the ROS generated, challenges the practicality of pursuing CYPs as biocatalysts in preparative-scale applications. [10]

An alternative consideration to circumvent the 'oxygen dilemma' is to engineer CYPs to use hydrogen peroxide (H₂O₂) or organic peroxides to "shunt" the substrate bound ferric heme via a Compound 0 (Fe(III)-OOH) intermediate, which, following protonation undergoes heterolytic cleavage of the O—O bond to generate Compound I. [10-12] Whilst few CYPs are efficient in the 'peroxide shunt', CYP152 members naturally use H₂O₂ as the terminal oxidant to carry out hydroxylation reactions. The CYP152A1 from Bacillus subtilis (P450BSB) and the CYP152B1 from Sphingomonas paucimobilis (P450SPa) were the first identified to be active in fatty acid hydroxylation (primarily forming β - and α -hydroxylation products, respectively) using solely H2O2 as a co-substrate in a reaction that is termed peroxygenase activity. [13,14] Subsequently, a CYP152 member found in the bacterium Jeotgalicoccus sp. ATCC 8456 was identified to be able to liberate CO2 and produce Cn-1 terminal olefins from fatty acid substrates using H₂O₂ as a co-substrate. [15] This decarboxylase activity is an attractive property for exploitation in sustainable manufacturing of drop-in biofuels, and other CYP152 members have been identified to display such activity. [15-20]

The CYP152L1 from Jeotgalicoccus sp. ATCC 8456 host strain, referred to as $OleT_{JE}$ is the most well characterised P450 decarboxylase capable of producing predominately terminal alkenes from saturated fatty acid substrates with alkyl chain lengths varying between C_{10:0} to C_{20:0}. [21,22] The catalytic mechanism of OleT_{JE} proceeds by first forming Compound I upon reaction with H2O2, which like canonical hydroxylating P450s abstracts a H atom from the bound substrate to generate an Fe(IV)-OH Compound II species. [23,24] In OleT enzymes, this Compound II species was found to be metastable on the order of hundreds of milliseconds as opposed to canonical P450s operating an oxygen rebound mechanism to hydroxylate the substrate, where Compound II is fleeting and thus experimentally challenging to trap. [24–26] This inherent stability of Compound II appears to be a defining factor in the decarboxylation chemistry of OleT_{JE}, enabling it to accept a further substrate electron, coupled by recruitment of a proton, to form Fe(III)-OH₂, concomitantly generating a substrate biradical or carbocation species that undergo O₂C-Cα bond cleavage releasing CO₂ and producing the C_{n-1} alkene. [24,27]

An X-ray crystal structure of $OleT_{JE}$ with a $C_{20:0}$ fatty acid bound has been determined to 2.5 Å resolution revealing the location of a pair of residues, Arg and Pro, located on the I helix with the polar carboxylic head-group of the fatty acid substrate acting as a hydrogen-bond (H-bond) acceptor from the guanidium group of the Arg to create an acid-base pair. [21] This interaction has also been reported in other CYP152 X-ray crystal structures determined with $C_{14:0}$, $9\text{-}cis\text{-}C_{16:1}$, $C_{16:0}$ and $9\text{-}cis\text{-}C_{18:1}$ bound fatty acid substrates [18,28–31], and is deemed to serve as the acid-base catalyst that drives proton abstraction and donation to activate the Fe(III) bound H_2O_2 facilitating heterolysis of the O—O bond and Compound I formation.

The Gram positive pathogenic bacterium *Staphylococcus aureus* possesses a CYP152 with decarboxylase activity. [19] Several studies with $OleT_{Sa}$ have been reported, including the application of small benzene containing molecules to enhance reactivity, [32] as well as protein

engineering on the proximal side of the heme to increase accumulation of Compound I. [20] Following the heterologous over-expression in Escherichia coli and purification of OleTSa we have identified that a monounsaturated fatty acid, elaidic acid (trans-C_{18:1}), is co-purified. The majority of past CYP152 studies have focused solely on using saturated fatty acids as substrate to investigate structure and mechanism. However, unsaturated fatty acids are both more common in nature and thus more likely to be biologically relevant, and are a major component of many renewable fatty acid feedstocks. [33] Recent studies have shown some, CYP152s are capable of carrying out decarboxylation reactions on unsaturated fatty acids, [31] highlighting the importance for further characterisation of CYP152s with unsaturated substrates. Herein we have investigated the thermodynamic, kinetic and structural properties of OleTSa and variants with the unsaturated elaidic acid and compared these with its saturated counterpart stearic acid (C_{18:0}). We show that OleT_{Sa} retains its decarboxylation activity to an equivalent degree as with a saturated fatty acid and thus allows the product profile of this CYP152 to be expanded to produce dienes.

2. Experimental

2.1. Synthesis and cloning of an $OleT_{Sa}$ vector for over-expression in Escherichia coli

The $OleT_{Sa}$ protein sequence (GenBank accession number: WP_049319149) was used to create codon optimised DNA for over-expression in *E. coli* and synthesised by Invitrogen. The synthesised product (1290 bp) was inserted into a pMA-RQ(Amp^R) vector and oligonucleotides carrying *NdeI* and *HindIII* restriction sites at the 5′ and 3′ ends, respectively, were synthesised (Merck) and used to amplify the $OleT_{Sa}$ DNA for subsequent ligation into a pET28a vector, under the control of the T7 promoter. This created an N-terminal His₆-tagged $OleT_{Sa}$ construct in which the His₆-tag could be cleaved using a thrombin recognition sequence following over-expression. Successful insertion of the $OleT_{Sa}$ between the *NdeI* and *HindIII* restriction sites of the pET28a vector was corroborated through DNA sequencing (Eurofins) using the T7 and T7 term sequencing primers.

2.2. Construction of site-directed variants of $OleT_{Sa}$

The following site-directed variants, L39F, L79T, F174A, I177A and N243A were constructed using a site directed mutagenesis strategy based on the Q5 PCR protocol. Non-overlapping oligonucleotide primers were designed and synthesised (Eurofins) with the desired base changes to create the respective OleT_{Sa} variants introduced at the 5'-end of the forward primer (Table S1). PCR mixes were prepared to a final volume of 50µl with 0.5µl of OleT_{Sa} template, 0.5µl each of the desired forward and reverse primers, 25µl of Phusion Flash High-Fidelity PCR master mix (ThermoFisher Scientific) and 23.5µl of water (Millipore). Mixtures were placed into a thermocycler, and the following method was used to obtain PCR product; 98 °C for 30 s, (98 °C for 10 s, y °C for 20 s, 72 °C for 165 s) \times 30, 72 °C for 300 s (y = annealing temperatures between 58 and 64 °C, depending on primers). DpnI (Thermo Fisher Scientific) was added directly to the PCR reaction mix following completion of the reaction cycle, and left to incubate at 37 °C for 2 h, followed by gel extraction and purification from an agarose gel. All gel-purified products were incubated at room temperature for 2 h with 8µl of a mix containing 10× T4 polynucleotide kinase (PNK) buffer, T4 PNK, 10× T4 ligase buffer and T4 ligase (all ThermoFisher Scientific), followed by transformation to E. coli TOP10 cells (Invitrogen). DNA sequencing (Eurofins) was used to confirm that the selected transformants contained clones carrying the desired site-directed mutant.

2.3. Over-expression and purification of $OleT_{Sa}$ and site-directed variants

The OleT_{Sa} pET28a vector (wild-type and variants) was transformed

into C43(DE3) E. coli cells, with the resulting transformants used to inoculate overnight precultures containing 10 ml of LB (Melford Chemicals) and 50µg/ml of kanamycin (Fisher Scientific). Shake flasks (2 L) were prepared containing 1 L of 2xYT media (Melford Chemicals) and supplemented with 500µM 5-aminolevulinic acid hydrochloride (Merck) and 100µM Fe(III) citrate (Sigma) to assist heme biosynthesis, and 50µg/ml of kanamycin. The overnight pre-cultures were used to inoculate each shake flask and growth continued at 37 °C with shaking at 180 rpm until an OD₆₀₀ of 0.8 was reached, on which induction of $OleT_{Sa}$ was initiated through the addition of isopropyl β -D-thiogalactopyranoside (Melford) to a final concentration of $250\mu M$ and the temperature reduced to 25 °C for overnight shaking. Cells were harvested (4000 g, 20 min, 4 °C) and the cell pellet resuspended in a minimal volume of Buffer A (50 mM Tris/HCl pH 7.5 buffer,20 mM imidazole and 750 mM NaCl). The resuspended cell suspension was lysed by passing three times through an Avenstein-C3 cell homogeniser, followed by pelleting the cell debris by centrifugation (40,000 g, 45 min, 4 °C). The clear red supernatant was loaded directly to a 5 ml Ni-NTA (Cytiva) column, followed by washing with 10 column volumes of Buffer A, after which a linear imidazole gradient was initiated using Buffer B (Buffer A with 500 mM imidazole). Fractions from the major eluting peak containing $OleT_{Sa}$, were pooled and concentrated to ~ 10 ml using centrifugal concentrators (Vivaspin 10 ka cut-off). At this point the N-terminal His6-tag was removed through addition of 1 KU of bovine thrombin (Merck) and incubation overnight at 16 °C. The overnight solution was clarified by centrifugation (4500 g, 10 min, 10 $^{\circ}$ C) followed by loading to a 5 ml Ni-NTA column and the flow through collected. A S200 Sephadex column (Cytiva) equilibrated in Buffer C (100 mM sodium phosphate pH 7.5, 750 mM NaCl) was used in the final purification step with a major peak eluting at ~75 ml consistent with a monomer species and fractions from this peak assessed for purity by SDS-PAGE. Lower yields were obtained for all variants, L39F (~7 mg/l), L79T (~2 mg/l), F80T (~4 mg/l), F174A and I177A (~5 mg/l), and N243A (\sim 3 mg/l) compared to the WT (15–20 mg/l).

2.4. Electronic absorption spectra

All electronic absorbance spectra of $OleT_{Sa}$ and variants were recorded using a Varian Cary 60 UV-visible spectrophotometer. Protein concentration was determined using an extinction coefficient (ϵ) at 280 nm ($\epsilon_{280} = 58,455 \, M^{-1} \, cm^{-1}$) that was calculated using ProtParam, [34] and heme concentration was determined using the low-spin Soret band at 418 nm ($\epsilon_{418} = 113,000 \, M^{-1} \, cm^{-1}$) [20] for fitting of fatty acid binding titrations. To obtain spectra of the ferrous carbon monoxide (CO) form of the $OleT_{Sa}$ samples, a few crystals of solid sodium dithionite (Fisher) were added directly to the cuvette and sealed with a rubber septum. Reduction to the ferrous state was confirmed by the acquisition of a spectrum before CO was bubbled into the cuvette using a needle attached to gas tight glass syringe (Hamilton).

2.5. Fatty acid binding titrations

Prior to titration experiments all $OleT_{Sa}$ samples were treated with a 5 M excess of H_2O_2 (33 % Merck) suspended in Buffer C and then applied to a desalting PD10 column to remove any co-purified fatty acid and unreacted H_2O_2 . Titrations were conducted in Buffer C using an $OleT_{Sa}$ concentration of $\sim 5\mu M$. Stock solutions of the saturated dodecanoic acid $(C_{12:0};$ Fisher), octadecanoic acid $(C_{18:0};$ Fisher) and icosanoic acid $(C_{20:0};$ Fisher) and unsaturated elaidic acid $(C_{18:1};$ Fisher) were prepared in a 70:30 ratio of ethanol and Triton X-100 (Merck). For icosanoic, octadecanoic and elaidic acids, 1 mM stock solutions were prepared and 1 μ l aliquots titrated into 1 ml of enzyme. For dodecanoic acid, stock solutions of between 1 and 1000 mM were prepared and titrated in 1 μ l aliquots to give the desired increase in concentration. All data from the titrations were fitted to a quadratic equation derived for tight binding substrates (the Morrison equation) [35] using SciPy curve fit.

2.6. Assays for identification of co-purified fatty acid and metabolic profiling

To identify the co-purified fatty acid, as purified OleT_{Sa} samples (475µM) were prepared by addition of a 5-fold molar excess of icosanoic acid to give a total volume of 550 µl. An equal volume of HPLC grade chloroform (ThermoFisher Scientific) was added and the solution centrifuged at 19,000 g for 25 min. The aqueous layer was discarded and ${\approx}300~\mu l$ of the organic layer was used for derivatisation and GC-MS measurement. To compare the metabolic profile between elaidic acid and stearic acid for WT and variants reactions of 200 μl were set up containing 25–95 μ M OleT_{Sa}, 500 μ M fatty acid, and 1000 μ M H₂O₂. The reactions were left to incubate at room temperature with gentle rocking for 30 min, after which a hexadecane internal standard (1000 μM) was added. The organic components of the reactions were then extracted by adding an equal volume chloroform, centrifuging for 2 min (19,000 g), and removing the organic layer. This extraction was repeated three times for before the resulting organic solution was concentrated to 200 μl under pressured air, followed by derivatisation and GC-MS analysis.

2.7. Gas chromatography mass spectrometry (GC-MS)

All samples for GC-MS were derivatised with 25 μL of BSTFA:TMCS (99:1) (Merck) and incubated at 60 °C for 20 min for trimethylsilylation. Samples were analysed with an Agilent 7890A gas chromatography system equipped with an Agilent 19091s-433 column (30 m \times 250 μm \times 0.25 μm) and an Agilent 5975C VL MSD triple axis detector, flow rate 1 ml/min. The oven was initially held at 40 °C for 5 min, then increased to 160 °C at a rate of 25 °C/min, then further increased to 240 °C at a rate of 2 °C/min where it was held for 15 min. Finally, the oven temperature was increased to 310 °C at a rate of 25 °C/min where it was held for 5 min. The MS of individual peaks were compared using the National Institute of Standards and Technology (NIST) MS search 2.0.

2.8. Temperature dependent UV-visible spectroscopy

Electronic absorbance spectra at different temperatures for the various OleT_{Sa} samples were measured on a SX20 stopped-flow spectrophotometer (Applied Photophysics, UK) attached to a water circulator for temperature control. The photodiode-array multi-wavelength unit and the internal trigger were used to collect spectra. The concentrations of both the high- and low-spin heme states at every temperature measured were calculated using the absorption coefficients of the Soret peak for pure high-spin $(\epsilon_{8394}=107~\text{mM}^{-1}~\text{cm}^{-1})$ and low-spin $(\epsilon_{394}=63~\text{mM}^{-1}~\text{cm}^{-1})$ as well as the 406 nm isosbestic point $(\epsilon_{406}=87~\text{mM}^{-1}~\text{cm}^{-1})$. [20] This enables the spin equilibrium constant (K) to be determined using the ratio of [high-spin]/[low-spin] at each temperature measured allowing for the construction of van't Hoff plots from which the enthalpy (Δ H) and entropy (Δ S) were determined by fitting to Eq. (1) using SciPy curve_fit.

$$lnK = -\frac{\Delta H}{RT} + \frac{\Delta S}{R} \tag{1}$$

where R is the gas constant (1.98 cal/(mol K)) and T is temperature (K). The Gibbs free energy (Δ G) for each OleT_{Sa} sample at 293 K was subsequently calculated using Eq. (2),

$$\Delta G = \Delta H - T \Delta S \tag{2}$$

and the equilibrium constant for the spin-shift equilibrium (K_{spin}) at the same temperature (293 K) determined by Eq. (3).

$$K_{spin} = e^{-\Delta G/RT} \tag{3}$$

The ΔG error was calculated using the propagation of errors using the covariance calculated form the van't Hoff plot fits.

2.9. Electron paramagnetic resonance (EPR) spectroscopy

A Bruker E500 X-band (9.35 GHz) EPR spectrometer combined with an Oxford Instruments liquid helium system was used to measure low temperature continuous wave EPR spectra. Samples consisting of as purified, $\rm H_2O_2$ treated and $\rm C_{20:0}$ bound WT $\rm OleT_{Sa}$ (final volume of 250 μl and a concentration of 200 μl in buffer C) were transferred to 4 mm O.D. quartz EPR tubes (Wilmad Glass, Buena, NJ) and frozen in a cooling bath consisting of methanol kept on dry ice (~ 195 K). Samples were measured at 20 K and 7 K at a range of microwave powers.

Instrument parameters to record spectrum were as follows: modulation frequency 100 kHz; modulation amplitude 10 G; receiver gain 60 dB; conversion time 80 ms; sweep time 81.92 s. All EPR spectra were simulated in EasySpin [36] in the MATLAB environment using the *pepper* routine and the *esfit* fitting procedure.

2.10. Stopped-flow absorbance spectroscopy

Transient kinetics of the reaction of H₂O₂ reacting with OleT_{Sa} was performed using a SX20 stopped-flow spectrophotometer (Applied Photophysics, UK) equipped with either a photodiode-array multiwavelength unit or a photomultiplier tube and thermostatted to 10 °C. All as purified OleT_{Sa} samples were prepared in Buffer D (100 mM sodium phosphate pH 7.5, 500 mM NaCl) to give a final concentration of \approx 5µM after mixing with H₂O₂. Final H₂O₂ concentrations ranged from 1000 μM – 16 μM after mixing. Data from the photodiode array (PDA) were fitted globally following singular value decomposition (SVD) analysis using Pro-K software (Applied Photophysics) to a sequential Bateman model (A to B to C). SVD decomposes the experimentally determined wavelength, time, absorbance matrix into three orthogonal matrices that partition spectral and kinetic information. The spectral matrix provides basic spectra which are not spectra of chemical intermediates but can be combined in a linear combination to form any spectrum in the data set. These matrices also constrain the number of chemical components that can be used in any model building. Once a model has been selected the base spectra and kinetic matrix, together with the "weighting matrix" may be combined to give actual spectra of intermediates and their time courses for formation and decay. Data from the photomultiplier tube (PMT) were the average of between 3 and 10 individual time courses and fitted to the sum of two exponentials allowing for both rate constants and the change in absorbance of the two phases to be obtained. To recreate the spectrum of Compound I, the change in absorbance corresponding to the faster of the two phases was corrected to account for the dead time of the stopped-flow instrument allowing for the corrected change in absorbance between the start and end of the faster phase to be subtracted from the SVD generated Compound II spectrum at all wavelengths measured. The dead time of the stopped-flow apparatus was determined by mixing ferrous horse heart myoglobin (Sigma-Aldrich) with known concentrations of CO. [37] This deadtime should not be confused with the flow time of the apparatus (\sim 2 ms). The dead time correction factor was based on the first order rate law (Eq. (4)).

$$A_t = A_0 e^{-kt} \tag{4}$$

where A_t is the amplitude at any given time (t), and A_0 is the absorbance at t=0. By using Eq. (4) and the determined deadtime of 1.2 ms, A_0 can be determined at each wavelength.

2.11. Crystallisation and structure determination

A Crystal Gryphon protein crystallisation pipettor (Art Robbins Instruments) was used for crystallisation screening of as purified $\mbox{OleT}_{Sa}.$ A protein concentration of 33 mg/ml was prepared in Buffer C and 200 nL dispensed onto either 200 or 400 nL precipitant solution from a commercial crystal screen (Molecular Dimensions and Hampton Research)

in a 96 well sitting-drop plate (MRC-plate; Molecular Dimensions). Screening was performed against >1000 known crystallisation conditions across several screens. A single crystal was formed from the Index crystal screen (Hampton Research), condition B12 (2.8 M sodium acetate trihydrate, pH 7.0), which was fished directly from the 96-well plate and flash-cooled in liquid nitrogen. X-ray diffraction data was collected remotely at beamline IO4 Diamond Light Source at 100 K and a wavelength of 0.95374 Å. Diffraction data were integrated, scaled and merged using the xia2 DIALS pipeline. [38] Data reduction and resolution estimates was carried out using Aimless in the CCP4i2 suite. [39] Structure determination was carried out by molecular replacement using MrBUMP [40] and automated model building with Buccaneer. [41] The search model identified by MrBUMP was PDB entry 5m0n, which is the X-ray structure of OleT_{JE} in complex with formate. [22] Structure refinement was carried out in Refmac5, [42] with model building between refinement cycles carried in Coot. [43] Ligand coordinates and restraints for C_n fatty acids (where n = number of carbons) were generated from SMILES strings using AceDRG [44] in the CCP4i2 suite and subsequently used for modelling and refinement in Coot and Refmac5, respectively A summary of X-ray data collection and refinement statistics are reported in Table 1.

3. Results

3.1. Electronic absorption spectra of as purified and H₂O₂ treated OleT_{Sa}

The electronic absorption spectrum of the as purified OleT_{Sa} is reported in Fig. 1A, together with the spectrum taken after addition of H₂O₂. As purified, the spectrum displays a broad Soret peak with clear wavelength maximum at 414 nm and a shoulder at 394 nm. A distinct absorbance band at ~650 nm is also present that is consistent with a charge transfer band arising from a thiolate high-spin Fe(III) heme iron (Fig. 1A). On addition of H2O2 the Soret band sharpens, increases in absorbance, and red shifts to a peak maximum of 418 nm (Fig. 1A). Furthermore, changes in the Q-band region occur with the formation of two peaks with wavelength maxima at 537 and 568 nm, and a notable decrease in intensity of the Cys-Fe(III) heme charge transfer band at 650 nm (Fig. 1A). Taken together, these observations are consistent with a transition from an as purified OleT_{Sa} species exhibiting mixed high-lowspin Fe(III) heme character to a species dominated by a low-spin Fe(III) heme, consistent with OleT_{Sa} co-purifying with a bound substrate, i.e. a fatty acid, that promotes high-spin heme character.

3.2. Identification of the co-purified fatty acid bound to $OleT_{Sa}$

Heterologous over-expression of CYP152s co-purifying with a bound substrate has been widely reported, including for OleT_{Sa}. [20] However,

Table 1Crystallographic processing and refinement statistics for as purified *S. aureus*OleT. Values in parenthesis are for the highest resolution shell.

Space group	P32 2 1
Unit cell (Å)	$a = 137.8, b = 137.8, c = 59.2, 90^{\circ} 90^{\circ} 120^{\circ}$
Resolution (Å)	68.99-1.83 (1.86-1.83)
Unique reflections	101,189 (4781)
Multiplicity	82.0 (81.1)
Completeness (%)	99.9 (100.0)
Mn(I/sd)	14.7 (0.1)
R _{merge}	0.24 (0.38)
Wilson B-factor (Å ²)	41.9 (10.7)
$CC_{1/2}$	0.99 (0.41)
Reflections used in refinement	57,102
R _{work}	0.164
R_{free}	0.194
RMSD bond lengths (Å)	0.014
RMSD bond angles (°)	2.43
Ramachandran most favoured (%)	98.6
PDB accession code	9RXH
Unique reflections Multiplicity Completeness (%) Mn(I/sd) R _{merge} Wilson B-factor (Ų) CC _{1/2} Reflections used in refinement R _{work} R _{free} RMSD bond lengths (Å) RMSD bond angles (°) Ramachandran most favoured (%)	101,189 (4781) 82.0 (81.1) 99.9 (100.0) 14.7 (0.1) 0.24 (0.38) 41.9 (10.7) 0.99 (0.41) 57,102 0.164 0.194 0.014 2.43 98.6

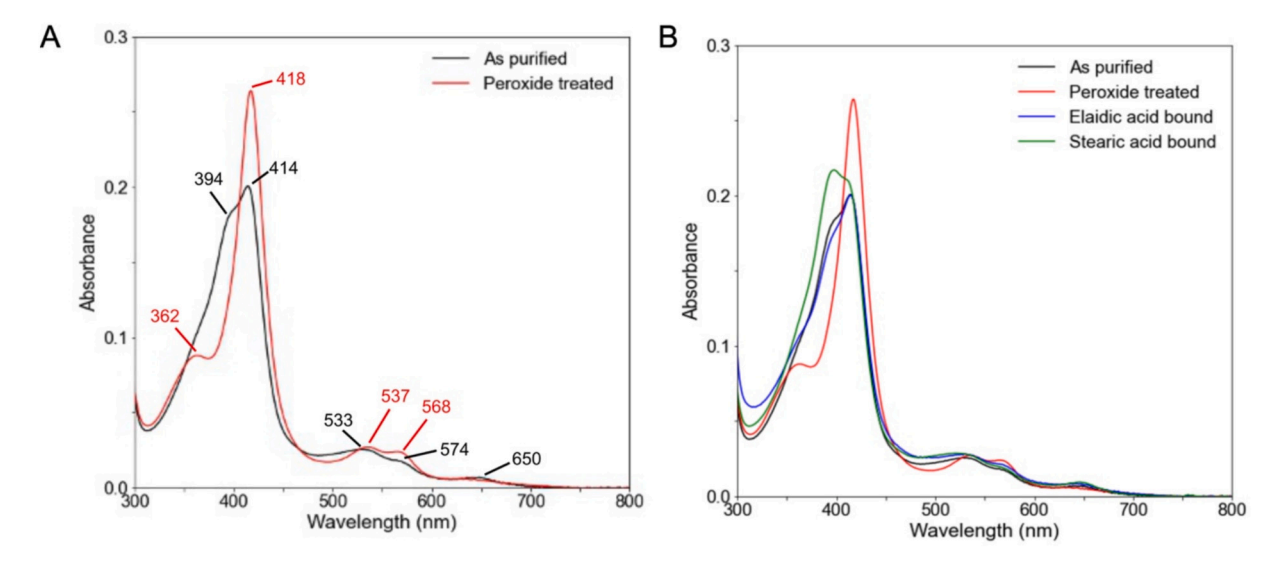


Fig. 1. Electronic absorption spectroscopy of $Olet_{Sa}$ at pH 7.5 A) UV-vis spectra of as purified and H_2O_2 treated $Olet_{Sa}$ with the respective wavelength maxima (nm) indicated. B) UV-vis spectra comparing the as-purified with the additions of saturated (stearic) and monounsaturated (elaidic) C18 fatty acids.

the chemical nature of the bound substrate in as purified CYP152 members is not routinely analysed. Multiple heterologous expressions of ${\rm OleT_{Sa}}$ consistently yielded spectra like that shown in Fig. 1A. To identify the co-purified substrate, we first incubated as purified ${\rm OleT_{Sa}}$ with a large excess of the saturated icosanoic acid (${\rm C_{20:0}}$), with the aim of displacing the co-purified substrate. A previous report has demonstrated using variable alkyl chain length saturated fatty acids, that icosanoic acid (${\rm C_{20:0}}$) has the highest binding affinity (${\rm K_d}=0.26\mu{\rm M}$) for ${\rm OleT_{Sa}}$. [20] Furthermore, icosanoic acid is not present in either *E. coli* or in growth media supplements. GC-MS analysis revealed the presence in the chromatogram of a peak possessing a mass spectrum with a

fragmentation pattern consistent with icosanoic acid and a second peak eluting at an earlier retention time than icosanoic acid was also present, with the fragmentation pattern of its mass spectrum being consistent with a monounsaturated $C_{18:1}$ fatty acid, with *trans-9*-octadecenoic acid (elaidic acid) being the closet match (Fig. S1). No other chromatogram peaks were identified as fatty acids. Therefore, heterologous expression and purification of $O(C_{18})$ yields a co-purified sample with a monounsaturated C18 fatty acid bound.

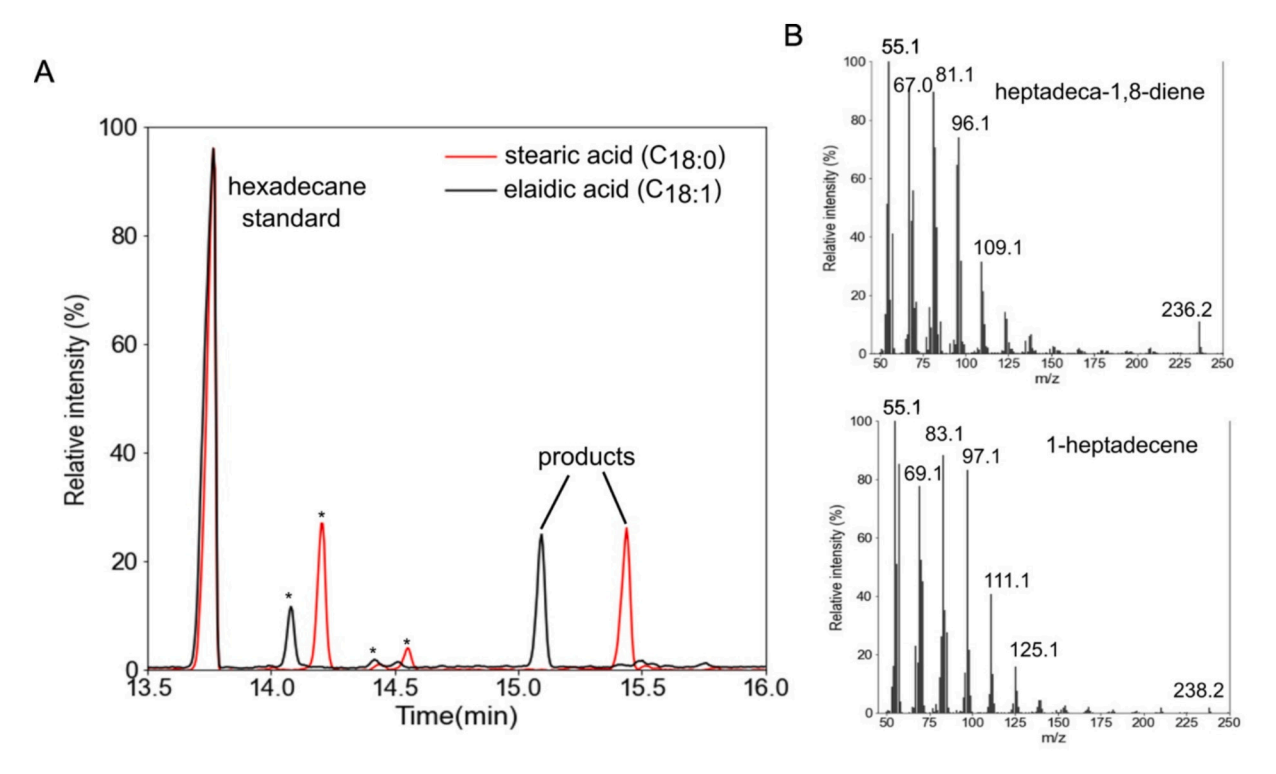


Fig. 2. GC-MS metabolic profiling of stearic and elaidic acids with $OleT_{Sa}$. A) GC-MS chromatogram of $OleT_{Sa}$ after extraction of samples into chloroform and BSTA/TMS derivatisation from turnover assays with stearic or elaidic acid. The * indicate impurities, with the peaks corresponding to products, which elute after the hexadecane standard labelled. B) MS of product peak peaks with charge series for elaidic acid (top) and stearic acid (bottom). A m/z difference of 2 is consistent with the two products identified.

3.3. Spectral changes and metabolic profiling of saturated and unsaturated C18 substrates

As much of the previously reported work with OleT homologs has had a focus on saturated fatty acids, we pursued comparing the spectral properties of OleTSa in the presence of a C18 saturated and monounsaturated fatty acid. Addition of approximately 5-fold molar excess of stearic (C_{18:0}) or elaidic (C_{18:1}) acid to the low-spin ferric heme state of OleT_{Sa} gave rise to the electronic absorption spectra reported in Fig. 1B. For both substrates a high-spin heme species contributes to the absorbance spectrum, with a split Soret peak most prominent in the case of stearic acid (Fig. 1B). On the other hand, elaidic acid, displays high spectral overlap with the as purified OleTsa. Addition of superstoichiometric amounts of H2O2 to either of the C18 fatty acid bound OleT_{Sa} samples led to the formation of the ferric low-spin heme form, *i.e.* demonstrating substrate turnover. To explore this further, metabolic profiling of OleT_{Sa} towards stearic and elaidic acid was analysed following turnover assays using GC-MS. Product peaks eluted after the hexadecane standard (Fig. 2A). The fragmentation pattern of the product peaks was consistent with the C_{18:1} reaction producing heptadeca-1,8-diene, and the $C_{18:0}$ reaction producing 1-heptadecene, a m/z difference of 2, as expected (Fig. 2B). Both the saturated and unsaturated fatty acids undergo similar levels of substrate conversion (~50 %) yielding 100 % of the decarboxylated products and no evidence for hydroxylated products. Likewise hydroxylated products were not detected in a previous study with OleTsa and stearic acid. [20] Therefore, these results indicate that a mechanism of Cβ hydrogen atom transfer by OleT_{Sa} remains operative with a C18 monounsaturated fatty acid bound with a diene product being formed.

3.4. Saturated versus unsaturated C18 in vitro binding affinities

Titration of stearic and elaidic acid to the low-spin ferric heme state of $OleT_{Sa}$ were conducted and monitored by electronic absorption spectroscopy (Fig. 3). By taking the difference absorbance (Abs_{396–419}

 $_{\rm nm}$) at each titration point, and calculating the fractional saturation, binding isotherms were constructed (*inset* Fig. 3) and fitted to yield the dissociation constants ($K_{\rm d}$) reported in Table 2. For comparative purposes, titrations were also conducted with the saturated fatty acids icosanoic acid ($C_{20:0}$) and dodecanoic acid ($C_{12:0}$), (Fig. 3) with the determined $K_{\rm d}$ values (Table 2) in good agreement with previous work on OleT_{Sa}. [20] For all fatty acids used, the titration data and fitting are consistent with a 1:1 stoichiometry of binding, despite variations in the appearance of the low- to high-spin spectral transitions (Fig. 3). From Table 2 it is apparent from the $K_{\rm d}$ that elaidic acid has a more than three-fold higher affinity than the saturated stearic acid and is also slightly higher in affinity than the saturated icosanoic acid ($C_{20:0}$).

3.5. Determining the low- to high-spin heme equilibrium constant for WT $OleT_{S\alpha}$

The titration data suggest that the alkyl chain length influences the spectral shifts of the low- to high-spin heme transition. In CYPs the lowto high-spin Fe(III) heme transition occurring on binding a substrate molecule is well documented and the spin-shift equilibrium constant $(K_{\rm spin})$ can be determined as a function of temperature. [45] Changes in the electronic absorption spectra between \approx 5 and \approx 42 °C for as purified (C_{18:1}) and stearic acid bound OleT_{Sa} are shown in Fig. 4 (C_{20:0}, C_{12:0} and H₂O₂ treated are shown in Fig. S2). The ratio of high- to low-spin species (K_{spin}) in each sample follows an Arrhenius dependence allowing van't Hoff plots to be constructed (insets Fig. 4) from which ΔH and ΔS can be determined. Subsequently ΔG and K_{spin} can be calculated at 293 K (Table 2). The $K_{\rm spin}$ values follow the trend $C_{20:0} >$ as purified $\approx C_{18:0} >$ C_{12:0} > H₂O₂ treated (Table 2). Therefore, despite the spectral differences of OleT_{Sa} in the presence of stearic acid compared to elaidic acid (Fig. 1B), this does not appear to be reflected in the determined $K_{\rm spin}$ values.

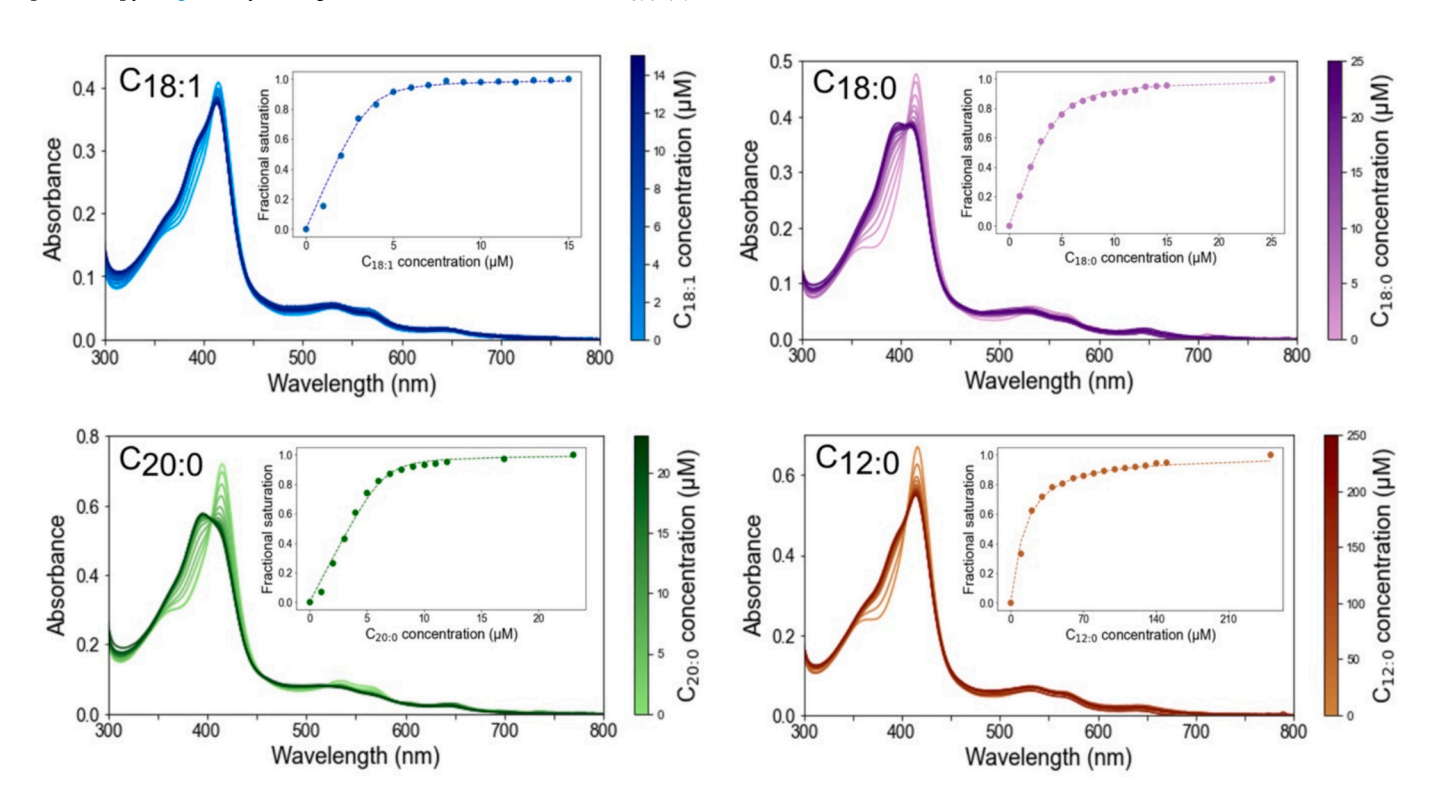


Fig. 3. Titration of WT $OleT_{Sa}$ with fatty acids monitored by electronic absorbance spectroscopy at pH 7.5. Binding isotherms (*insets*) constructed from the spectral changes can be fitted (dashed line) using a quadratic function to yield dissociation constants (K_d) reported in Table 2.

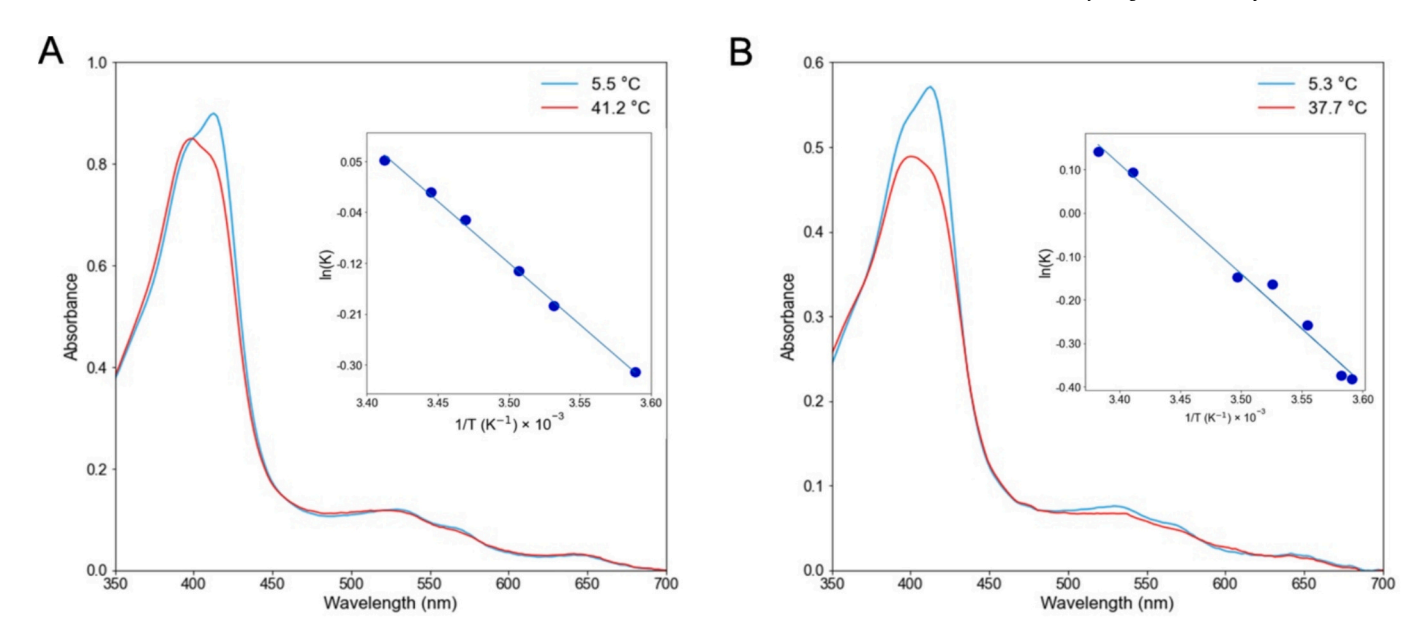


Fig. 4. Temperature dependence of the $OleT_{Sa}$ electronic absorption spectrum. A) as purified ($C_{18:1}$ bound) and B) with stearic acid ($C_{18:0}$) bound at two temperatures. *Insets*, temperature dependence of the spin-equilibrium constant (K_{spin}) with the blue line a linear fit to the data points (blue circles) to derive the thermodynamic parameters reported in Table 2. (For interpretation of the references to colour in this figure legend, the reader is referred to the web version of this article.)

3.6. EPR spectroscopy of $OleT_{Sa}$

The low- and high-spin heme species evident from electronic absorption spectroscopy were further investigated by EPR spectroscopy. Continuous wave X-band EPR spectra of as purified ($C_{18:1}$ bound), $C_{20:0}$ bound and H_2O_2 treated $OleT_{Sa}$ samples were measured and are reported in Fig. 5. Under non-saturating conditions (20 K and 0.5 mW power) all samples showed a complex mixture of rhombic ($g_{av}\approx 2.23$) low-spin EPR signals (Fig. 5A, full EPR spectra at 20 K and 7 K are presented in Fig. S3) The as purified spectrum could be simulated using two rhombic g-tensors (Fig. 5A and Table 3). The H_2O_2 treated sample presented a slightly more complex spectrum consisting of four rhombic g-tensors (Fig. 5A and Table 3) and the addition of icosanoic ($C_{20:0}$) acid yielded a slightly different spectrum from the H_2O_2 treated spectrum, containing four components with similar g-tensors to those in the H_2O_2 treated sample but with different proportions of each (Fig. 5A and Table 3). These low-spin heme species have g values consistent with other CYPs

[46] including $OleT_{JE}$ [21] and are a consequence of a proximally coordinated Cys thiolate heme and a strong distal ligand. The number of gtensors determined for the H_2O_2 treated $OleT_{Sa}$ (substrate free) matches that for substrate free $OleT_{JE}$ [21] with near identical g values for each species. The number of low-spin species decrease for the as purified $OleT_{Sa}$ indicating that elaidic $(C_{18:1})$ acid creates more ordered heme site, in contrast to icosanoic acid $(C_{20:0})$ where increased heterogeneity of low-spin species is observed (Table 3).

Measurements at lower temperature (7 K) revealed the presence of additional high-spin species (Fig. 5B) in all three samples. The as purified state contained features at g = 7.88, 6.02 and 4.27. The g = 4.27 feature is typical for non-specific non-heme iron and thus not further considered. The g = 7.88 and g = 6.02 features likely originate from mg = +/- 1/2 intra-doublet transitions of two different S = 5/2 species with different rhombicities with E/D values of \approx 0.1 and \approx 0, respectively. The g = 7.88 feature is consistent with a high-spin species (g = 7.76) identified in OleT_{JE} with icosanoic acid bound. [21,22] For the g

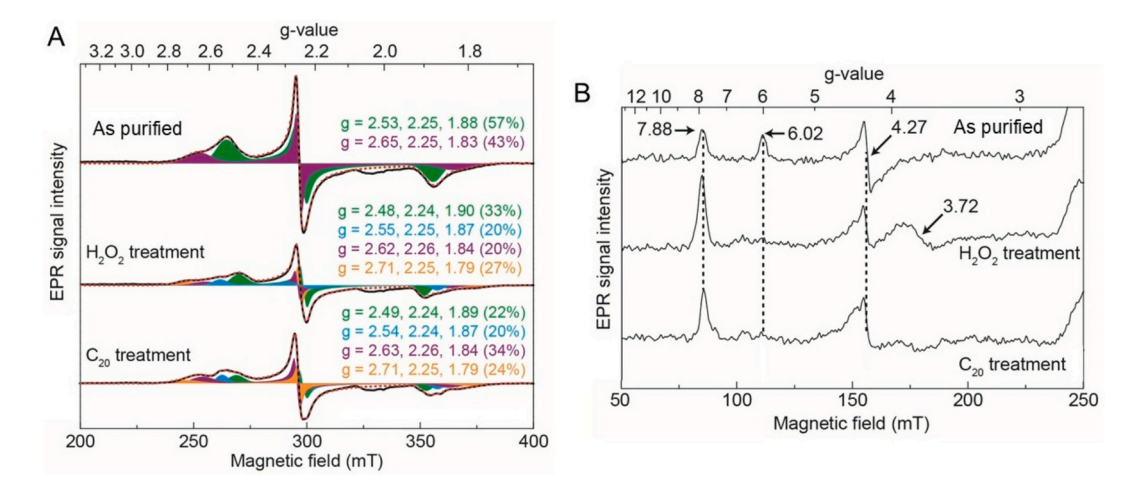


Fig. 5. X-band EPR spectroscopy of $OleT_{Sa}$. A) EPR spectra of various samples of $OleT_{Sa}$ measured at 20 K and 0.5 mW power. Experimental spectra are shown as black solid lines, simulations as red dotted lines, and individual component simulations as green, blue, purple and orange shaded areas with the component g-values and proportions (%) indicated. B) EPR spectra of $OleT_{Sa}$ measured at 7 K and 1 mW power focusing in on the high-spin heme signals. (For interpretation of the references to colour in this figure legend, the reader is referred to the web version of this article.)

=6.02 feature, this likely arises from Cys thiol heme coordination, and has been previously reported for some variants of OleT_{JE} which have a propensity to protonate the Cys-heme thiolate as evidenced by an increased proportion of the P420 species in the Fe(II)-CO absorption spectrum. [22] We note for OleT_{Sa} a significant P420 band in the Fe(II)-CO spectrum (Fig. S4). Interestingly, a high-spin feature is also observed for the H_2O_2 treated sample. Based on the determined K_{spin} value for H_2O_2 treated OleT_{Sa} (Table 2), the low-spin heme species is favoured. However, the slow freezing must somehow contribute to the trapping of some higher rhombicity (g = 7.88) species which also now causes formation of a feature at g = 3.72, likely attributable to the $m_S = +/-1/2$ intra-doublet transition of the same S = 5/2 species giving rise to the g = 7.88 feature. Addition of icosanoic acid ($C_{20:0}$) populates, the g = 7.88 feature, but there is loss of the g = 3.72 feature (Fig. 5B).

3.7. Stopped-flow reaction kinetics of as purified OleT_{Sa} with H₂O₂

To investigate the mechanism of $OleT_{Sa}$ with an unsaturated fatty acid the kinetics of the reactions of H_2O_2 with as purified $OleT_{Sa}$ ($C_{18:1}$) and for comparison with stearic acid ($C_{18:0}$), were followed by stoppedflow spectroscopy. In the presence of either fatty acid, $OleT_{Sa}$ displays a rapid optical transition (Fig. S5) consistent with the static spectra

(Fig. 1A). At low concentrations of H₂O₂ this transition occurred in two phases, with global fitting analysis revealing an intermediate, the spectrum of which conformed to that expected for a CYP152 Compound II (i.e. Fe(IV)-OH), [24] with a red shifted and lower molar extinction Soret maximum of 421 nm, relative to the low-spin Fe(III) heme (Figs. 6A and S5). No spectral evidence of a Compound I species could be seen when mixing with low concentrations of H₂O₂, indicating Compound I formation is much slower than its decay. Subsequently, Compound II decayed to the low-spin ferric heme form with a H2O2 concentration independent rate constant (k_3) of 62 (3.9) s⁻¹ with as purified $(C_{18:1})$ and 55 (4.8) s⁻¹ with stearic acid $(C_{18:0})$. At high H_2O_2 concentrations, the global fitting analysis revealed that the starting spectrum contained some Compound I-like features, which were more pronounced for the as purified OleT_{Sa}, and included a distinct band centred close to 700 nm and a split Soret peak with bands at 370 and 417 nm (Fig. 6B and C).

To capture a pure spectrum of Compound I is difficult due to the rapidity of the decay, the diode array does not provide sufficient data in the first few milliseconds to provide a reliable spectrum. A deuterated icosanoic ($C_{20:0}$) substrate has previously been used with both $OleT_{Sa}$ [20] and $OleT_{JE}$ [23,24] slowing the decay of Compound I owing to a strong KIE and thereby facilitating spectral capture using

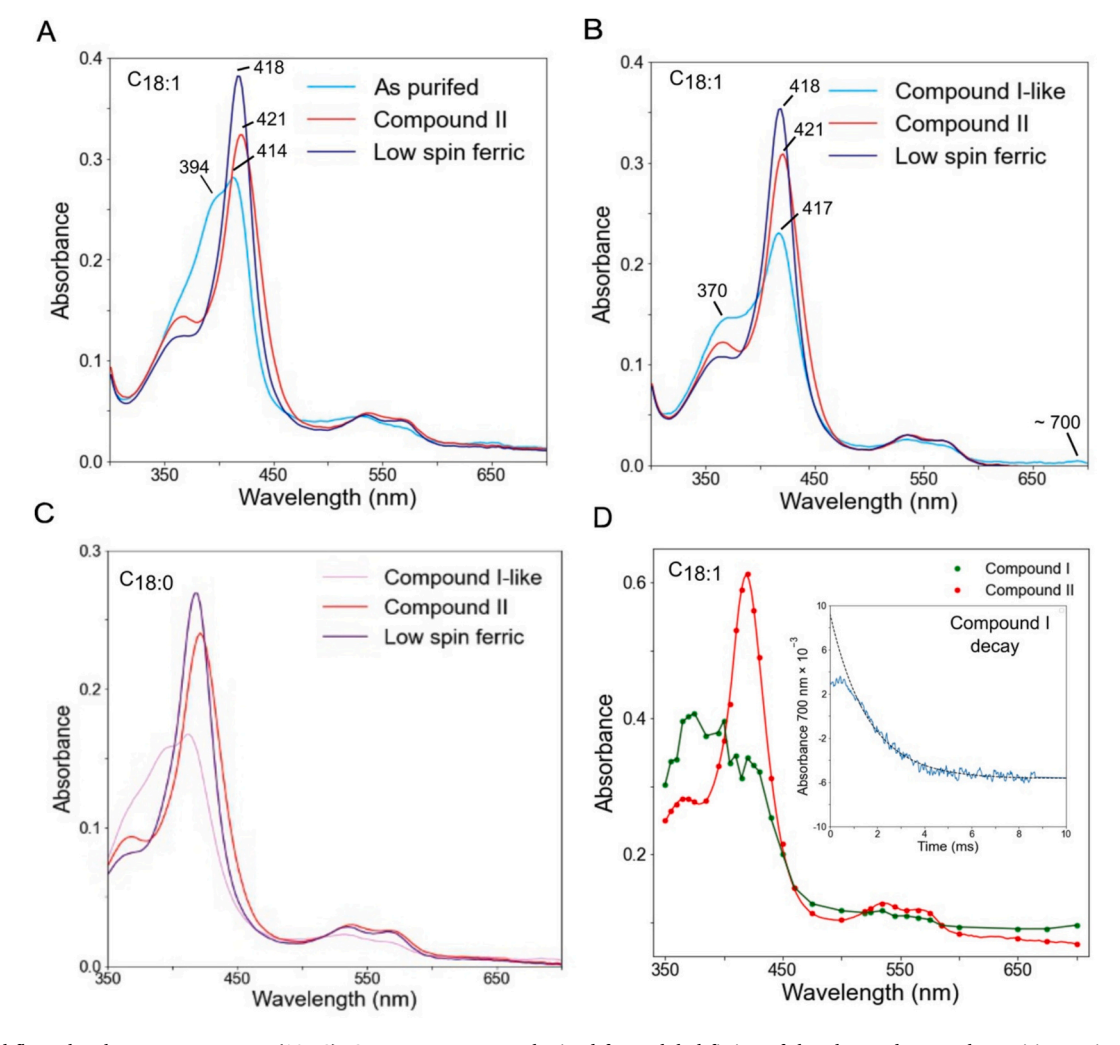


Fig. 6. Stopped-flow absorbance spectroscopy (10 °C). Component spectra obtained from global fitting of the observed spectral transitions using the PDA at low (15.5μM after mixing) and (B) high (1000μM after mixing) H_2O_2 concentrations for as purified ($C_{18:1}$) $OleT_{Sa}$ and (C) stearic acid ($C_{18:0}$) bound. Soret wavelength maxima for the various species are indicated, and a low intensity feature at ~700 nm assigned to Compound I. D) A point-by-point construction of the Compound I spectrum for as purified $OleT_{Sa}$ obtained by using the dead time corrected change in amplitude (see Experimental). *Inset* the PMT trace (blue) recorded at 700 nm for Compound I decay, with the black dashed line an exponential fit to the data with $k = 625 \text{ s}^{-1}$ (see Experimental section). (For interpretation of the references to colour in this figure legend, the reader is referred to the web version of this article.)

multiwavelength methods. We demonstrate an alternative method which avoids the use of expensive deuterated substrates, and any confounding issues which may result from this, and instead use point-bypoint spectral accumulation of the as purified OleT_{Sa}. Examination of the reaction with H₂O₂ concentration using the higher time resolution PMT allowed us to examine the spectral distribution of the faster of the two phases (i.e. the likely decay of Compound I to II) by measuring the amplitude of this phase across many wavelengths between 350 and 700 nm (e.g. inset Fig. 6D). Correcting this amplitude for the deadtime of the stopped-flow (determined to be 1.2 ms), and subtracting this corrected amplitude from the SVD generated Compound II spectrum (Fig. 6D) at each wavelength measured, allows us to construct the Compound I spectrum depicted in Fig. 6D for the as purified (C18:1) OleTSa. This point-by-point constructed Compound I spectrum (Fig. 6D) is consistent with both the global fitting analysis and published spectra obtained using a PDA for CYP152 peroxygenases when using a perdeuterated C_{20:0} substrate. [20,24] Thus, the faster phase seen at high H₂O₂ concentration, may be confidently assigned to the decay of Compound I with a rate constant (k_2) with a lower limit of 625 s⁻¹ (inset Fig. 6D) for the as purified $(C_{18:1})$.

Returning to the low H₂O₂ concentration regime, we observed for both saturated and unsaturated fatty acids the rate constant for the formation of Compound II (k1) was H2O2 concentration dependent (Fig. 7A). In this regime $k_2 >> k_1$, and therefore no evidence for a Compound I species is detected. Thus, the second order rate constant k₁ is assigned to the reaction (binding) of H₂O₂ with ferric fatty acid bound enzyme, yielding second-order rate constants (k₁) of $6.5 \times 10^5 \, \text{M}^{-1} \, \text{s}^{-1}$ and $3.7 \times 10^5 \,\mathrm{M}^{-1} \,\mathrm{s}^{-1}$, for $C_{18:1}$ and $C_{18:0}$, respectively The y-intercept taken from the fit to the data in Fig. 7A ($C_{18:1}$ bound) yields a k_{-1} of 3 s⁻¹, which can be assigned to the dissociation rate of the bound H₂O₂ from Compound 0 (Fe(III)-OOH) before formation of Compound I. With $C_{18:0}$ a higher k_{-1} is determined $\sim 14 \text{ s}^{-1}$ resulting in a lower concentration of Compound 0 and consequently a lower population of Compound I. Attempts to measure the decay of Compound I under the experimental conditions described to measure Compound I decay with C_{18:0} bound were thus unsuccessful. Taken together these stopped-flow data combined with the metabolic profiling data (Fig. 2) are consistent in describing a reaction mechanism for OleT_{Sa} depicted in Fig. 7B and demonstrate that as purified OleTSa is capable of decarboxylase activity with a bound monounsaturated C_{18:1} fatty acid to produce a C_{17:2} diene product.

3.8. X-ray crystal structure of as purified $OleT_{Sa}$

To visualise the interaction of a $C_{18:1}$ fatty acid with $OleT_{Sa}$ we

turned to X-ray crystallography. Despite extensive crystallisation efforts only a single diffraction quality crystal of as purified OleT_{Sa} could be obtained from one commercial screening condition in a 96-well robot plate. Subsequent scaling up procedures of the identified condition failed to yield further crystals. Nevertheless, a diffraction data set was collected from this single crystal and the X-ray structure of as purified OleT_{Sa} was determined by molecular replacement and refined to 1.83 Å resolution (Table 1). One protein molecule was identified in the crystallographic asymmetric unit, with the 2Fo-Fc density map enabling a complete model to be built starting at the N-terminal Gly2 and ending at the C-terminal residue, Val429. Refinement statistics and model quality are reported in Table 1. The $\mbox{Ole} T_{Sa}$ structure reveals the common CYP fold comprising a triangular prism shape made-up of predominately α -helices, with some β -sheet regions (Fig. 8A). Using a recently devised unifying secondary structure annotation to describe the anatomy of CYP families (both eukaryotes and prokaryotes) [47], we have identified in the OleT_{Sa} X-ray structure 17 helices (A', A, B, B', B", C, D, E, F, G, H, I, J, K, K', K", L) and 3 sheets each consisting of two β-strands (β 1–1, β 1–2, $\beta 2-1$, $\beta 2-2$, $\beta 3-1$, $\beta 3-2$) (Fig. 8A).

The *b*-type heme group can be modelled in two conformations as evidenced from the positive and negative density features in the F_0 - F_c omit map located at the two vinyl groups and methyl groups 1 and 3 (Fig. 8B). The two conformers are related by a 180° rotation along a plane of symmetry and based on occupancy refinement are of equal population (Fig. 8B). Such a phenomenon has been reported for the CYP121 from *Mycobacterium tuberculosis* [48] and recently for a CYP152 OleT from *Lacicoccus alkaliphilus*. [49] The heme-Fe is coordinated on the proximal face by Cys367 (2.2 Å), and a H_2O molecule at a distance of 2.2 Å has been modelled into the density on the distal face (Fig. 8B). A second H_2O molecule is found within the distal heme pocket and is within H-bonding distance (2.9 Å) of the coordinating heme-Fe H_2O (Fig. 8B) as well as the nitrogen atom NH2 (3.3 Å) of the guanidium group of the I helix Arg246 side chain (Fig. 8B).

In the distal heme pocket, two F_o - F_c density features were visible that cannot be accounted for by the protein (Fig. 9A). One displays long continuous electron density that snakes away from the distal heme pocket traversing a largely hydrophobic cavity towards sheets 1 and 2 (Fig. 8A). The second F_o - F_c feature is in the vicinity of the conserved I helix Arg/Pro motif (Fig. 9B). Based on the GC-MS analysis, we modelled into the long electron density feature a 9-trans- $C_{18:1}$ fatty acid (elaidic acid). Longer alkyl chain fatty acids e.g. C20 did not fit into the density, and neither could a 9-cis- $C_{18:1}$ fatty acid (oleic acid). In the refined X-ray structure, the trans-double bond lies underneath the side chains of Phe174 (helix F) and Ile177 (F/G loop connecting helices F and G). The carboxylic head group of the fatty acid lies over pyrrole ring IV of the

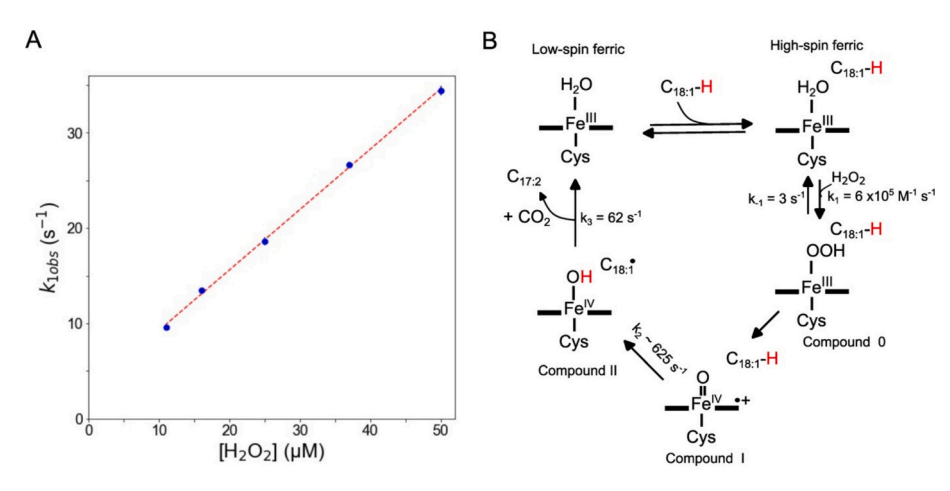


Fig. 7. H_2O_2 binding kinetics and reaction mechanism of $OleT_{Sa}$. A) Pseudo-first order rate constants (k_{1obs}) determined at low H_2O_2 concentrations when $k_2 >> k_1$. Data points fitted to a linear function to yield a second-order rate constant (k_1) for H_2O_2 binding, determined by the slope, and an off-rate (k_{-1}) taken from the y-intercept. B) Kinetic parameters determined from stopped-flow data that are consistent with the mechanism described for as purified $(C_{18:1})$ $OleT_{Sa}$.

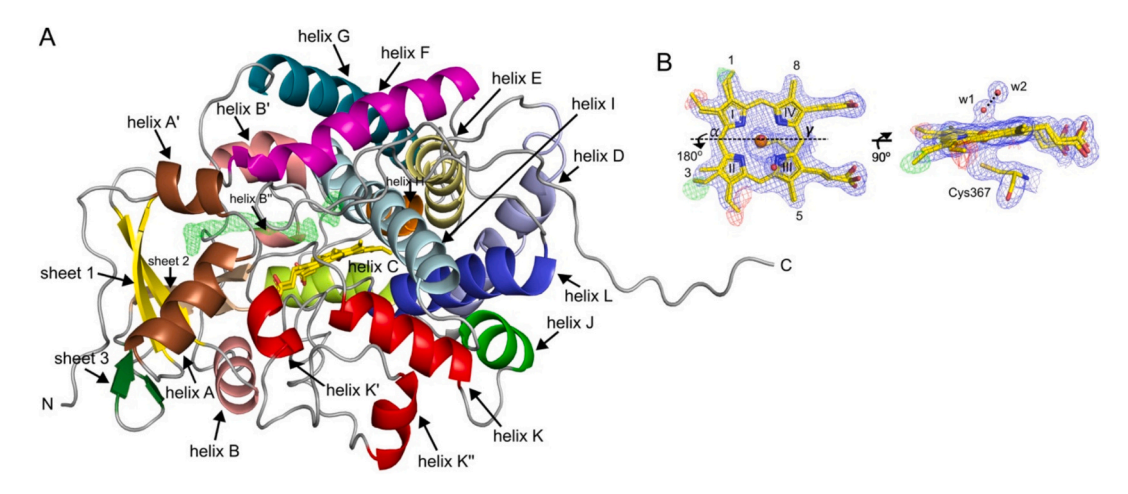


Fig. 8. X-ray crystallography. A) Cartoon representation of the X-ray crystal structure of as purified $OleT_{Sa}$. The N- and C-terminus are indicated together with the secondary structure elements that form the CYP152 fold, with the heme shown in stick representation. Two F_o - F_c density map features (green mesh) contoured at 5σ are in a cavity stretching from the distal face of the heme to sheets 1 and 2. B) A $2F_o$ - F_c density map (blue mesh) contoured at 1.2σ for the heme (sticks). The F_o - F_c density map (green positive and red negative densities) contoured at $+/-3.0\sigma$ is also shown to indicate the presence of two heme conformers rotated along the two-fold $C\alpha$ and $C\gamma$ symmetry axis. The methyl groups for one heme conformer are labelled. H-bonded distal heme pocket waters (w) are represented as red spheres. (For interpretation of the references to colour in this figure legend, the reader is referred to the web version of this article.)

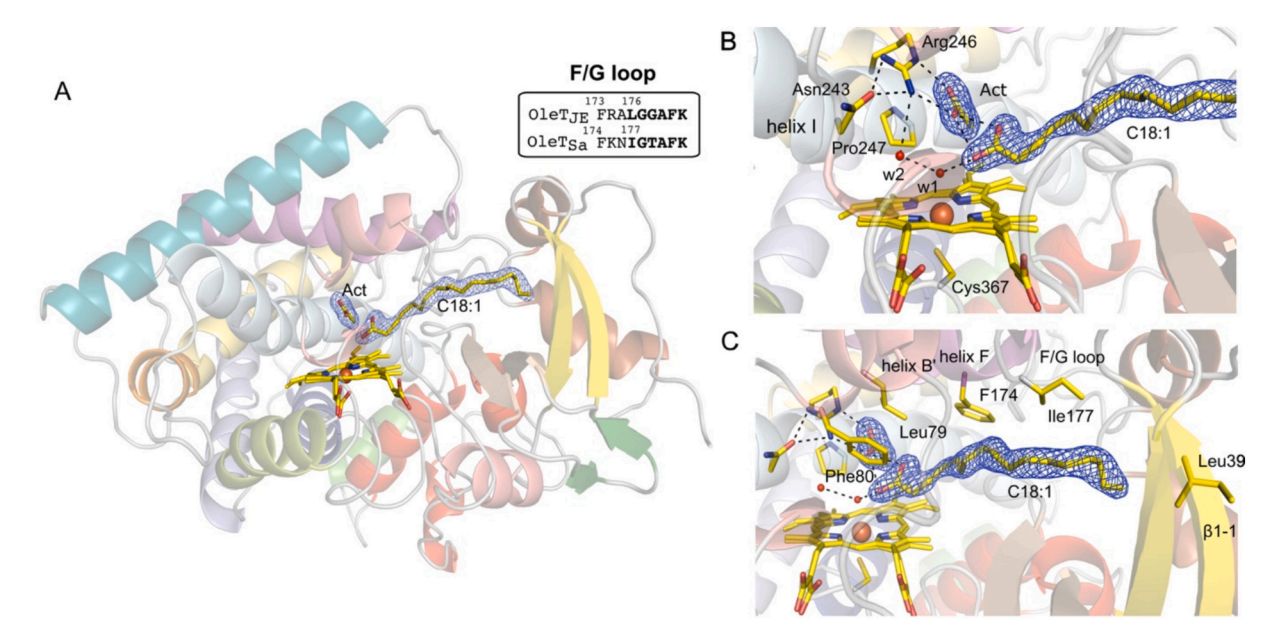


Fig. 9. Substrate interactions and variants. A) Overview of the modelled *trans*-9-octadecenoic acid (18:1) and acetate ion (Act) in the CYP152 fold. The $2F_0$ - F_c density is contoured at 1.5σ and represented as a blue mesh. The cartoon secondary structure colour scheme is identical to Fig. 8. Inset, comparison of sequence between $OleT_{JE}$ and $OleT_{Sa}$ in the vicinity of the F/G loop (bold). B) The intra and intermolecular I helix hydrogen bonding interactions (black dashed lines) and H-bond interactions with the carboxylic head group of the *trans*-9-octadecenoic acid. C) Location of the hydrophobic residues in the substrate cavity that were substituted to create the respective site-directed variants described in the main text. (For interpretation of the references to colour in this figure legend, the reader is referred to the web version of this article.)

porphyrin (Fig. 9B), with one of the oxygen atoms of the carboxylate group (O2) participating in a H-bond interaction (2.7 Å) with the heme-Fe coordinating $\rm H_2O$ molecule (Fig. 9B). Noting that the crystallisation conditions contained a high concentration of sodium acetate, we modelled into the second distal heme pocket $\rm F_0\text{-}F_c$ density feature an acetate ion and refined it with full occupancy (Fig. 9A). Both O atoms of the acetate ion act as H-bond acceptors for the nitrogen atoms of the NH2 (3.0 Å) and Ne (2.9 Å) of the Arg246 guanidinium group (Fig. 9B). The protonatable O atom of the acetate ion has further scope to be involved in a H-bond network with the carboxylic group of the modelled fatty acid (Fig. 9B). Thus, the X-ray crystal structure of the as purified OleT_{Sa}, suggests that the high concentration of acetate ions in the

crystallisation buffer competes for the carboxylic binding site of the fatty acid substrate and disrupts the catalytic acid:base pair. Consequently, the bound fatty acid slides back along the cavity, to take up a position which is most likely non-productive. This demonstrates that for alkyl chains of < C20 there is scope within the cavity for substrate dynamics. Furthermore, the position of the acetate ion in the distal heme pocket provides structural insight into the use of a 'decoy' molecule to initiate catalytic activity of non-native substrates in CYP152 members. [50]

3.9. Electronic absorption spectroscopy of as purified $OleT_{Sa}$ variants

The X-ray crystal structure of OleT_{Sa} with elaidic acid (C_{18:1}) bound

demonstrates that there is scope for substrates to slide along the substrate channel. To explore further this aspect of substrate binding and effect on reactivity, we generated a suite of site-directed variants at selected locations within the channel each positioned in van der Waals contact with the alkyl chain starting with Leu39, then Phe174 and Ile177 positioned on the extended F/G helix loop region, and Leu79 found in the distal heme cavity (Fig. 9C). A final variant at the Asn243 position was constructed, which is located on the I helix and is noted to participate in side chain H-bonding interactions with the catalytic Arg246 (Fig. 9B). These polar interactions could have a stabilising influence on the side chain position adopted by Arg246 which together with the I helix Pro247 is important for orientating the polar head group of the fatty acid and catalysis. All variants over-expressed in low yields and were deemed less stable than the WT OleT_{Sa} as evidenced by their gradual precipitation over time. Following purification, only the L39F and L79T variants displayed electronic absorbance spectra exhibiting a Soret region indicative of a low/high-spin Fe(III) heme mix, which on addition of H₂O₂ converted to a low-spin form (Fig. S6) The remaining variants exhibited electronic absorption spectra after purification that were most consistent with a low-spin Fe(III) heme species (Fig. S6), that on reduction bound CO (Fig. S7).

3.10. In vitro fatty acid binding to $OleT_{Sa}$ variants

From the initial purification of the variants only the L39F and L79T showed evidence of substrate binding. In vitro testing, initially with icosanoic (C_{20:0}) acid, because it gave the greatest spectral shift with the WT protein (Fig. 3), was confirmatory in that the L39F and L79T variants could bind a fatty acid with only a minimal effect on the determined K_d compared to the WT (Fig. 10 and Table 4). Although not evident from the as purified batch, the N243A and I177A variants did display spectral changes on addition of icosanoic ($C_{20:0}$) acid (Figs. 10 and S8) that were consistent with specific binding allowing a K_d to be determined (Table 4), whereas the F174A variant did not. However, the Soret spectral change is significantly suppressed compared to WT and the L39F and L79T variants (Fig. 10), with the changes observed more like with the shorter alkyl chain dodecanoic ($C_{12:0}$) acid (Fig. 3). This observation also coincides with a lower $K_{\rm spin}$ value and calculated percentage of high-spin heme for the N243A variant compared to the L39F variant which is closer to WT OleT_{Sa} (Table 4, Fig. S2). For the variants that showed spectral change on titration with icosanoic acid (C_{20:0}) titrations with stearic (C_{18:0}), and elaidic (C_{18:1}) acids were carried out. The I177A and N243A variants showed no spectral changes, whereas the

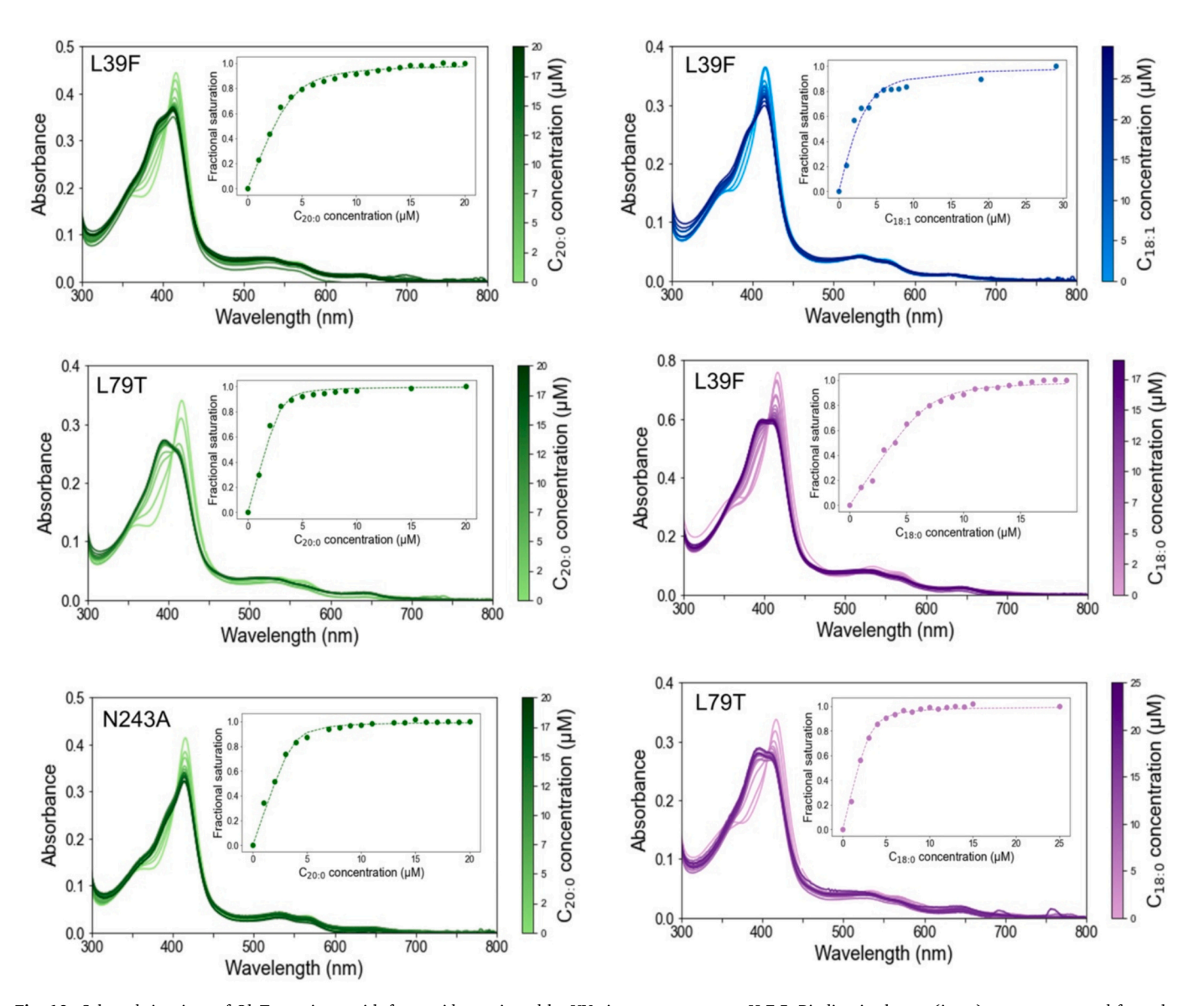


Fig. 10. Selected titrations of $OleT_{Sa}$ variants with fatty acids monitored by UV-vis spectroscopy at pH 7.5. Binding isotherms (*insets*) were constructed from the spectral changes and fitted (dashed line) using a quadratic function to determine K_d values reported in Table 4.

L39F gave similar spectral shifts as the WT (Fig. 10) with a marginally elevated K_d value (Table 4). For the L79T variant only stearic acid gave a spectral shift, which is similar to the WT and has a K_d reported in Table 4.

3.11. Metabolic profiling and kinetics of the site-directed variants

Metabolic profiling analysed by GC-MS was conducted with elaidic (C_{18:1}) and stearic acid (C_{18:0}) with all variants, regardless of whether a spectral change in their presence was observed. No evidence from the chromatogram of mixed product formation was observed, with all variants producing the expected decarboxylated product based on the bound fatty acid in the turnover assays. However, it was evident that the I177A and N243A variants produced 50-70 % less product compared to WT and the other variants. Based on the C18 binding data (Fig. 10) only the L39F variant was suitable for stopped-flow studies with the two C18 fatty acids. The resulting component spectra at low and high H₂O₂ concentrations, clearly show a Compound II species, (Fig. S9) indicative of oxygen rebound avoidance and decarboxylation as is evident from the metabolic profiling. The second-order rate constant of H₂O₂ binding (k₁) to the L39F variant is similar to that of the WT for $C_{18:0}$ (4.0 × 10⁵ M⁻¹ $\rm s^{-1}$ vs $\rm 3.7 \times 10^{5} \, M^{-1} \, s^{-1}$); for $\rm C_{18:1}$ the rate is decreased compared to the WT $(4.1 \times 10^5 \text{ M}^{-1} \text{ s}^{-1} \text{ vs } 6.5 \times 10^5 \text{ M}^{-1} \text{ s}^{-1})$ resulting in Compound I being less populated. The decay of Compound II to the ferric resting state is unaffected, with k_3 values of 75.4 (9.4) s^{-1} and 58.4 (9.6) s^{-1} .

4. Discussion

The co-purification of endogenous substrates with CYPs has long been recognised. For many years the presence of these 'impurities' unknowingly hindered the progress of identifying the existence of Compound I in CYPs, largely due in many cases to the absence of any spectral signatures, alerting to their presence. [51] In the cases of many of the reported WT OleT members a fatty acid is co-purified following heterologous expression and is spectroscopically detectable by a broad Soret peak that is representative of a low- to high-spin Fe(III) heme equilibrium. However, the identification of the co-purified fatty acid in CYP152s is never reported. In the present work we have identified a monounsaturated fatty acid bound to OleT_{Sa} following purification, which based on GC-MS and X-ray crystallography data is most consistent with trans-9-octadecenoic acid (elaidic acid; C18:1), which can be processed to form a diene product, heptadeca-1,8-diene (Fig. 2). Fatty acid content varies across bacteria. In E. coli around 60 % of the fatty acid distribution arises from $C_{12:0}$ (9 %), $C_{14:0}$ (12 %) and $C_{16:0}$ (35 %) with C_{18:0} and C_{18:1} making up 5 and 7 %, respectively. [52] Notably, a C_{20:0} fatty acid which has been used for much of the kinetic, mechanistic and structural studies on OleT members is not detected in E. coli, [52] but is present in Jeotgalicoccus sp. ATCC 8456 [15] and S. aureus. [53]

The EPR spectra in the presence of bound fatty acids are a complicated mix of low- and high-spin heme species (Fig. 5). This is also the case for the H_2O_2 treated sample that from the determined K_{spin} value (Table 2) is low-spin dominated. However, we note that the presence of high-spin EPR signals amongst CYP152 members could be exclusive to those that act as decarboxylases [21,22] as opposed to CYP152K6 that hydroxylates a substrate. [18] A further distinguishing feature between decarboxylases and hydroxylases is that based on the proposed kinetic mechanism [24], a Compound II species is detectable spectroscopically and relatively stable in comparison to CYP hydroxylases. Therefore, decarboxylase activity affords an opportunity to subject CYP152 members with a fatty acid bound to stopped-flow kinetic studies with H₂O₂, where the capture of a Compound II spectrum provides an early indication that decarboxylase activity prevails over hydroxylation. This indeed turns out to be the case with $OleT_{Sa}$ as purified with a transstereoisomer of a $C_{18:1}$ fatty acid, which incidentally the \emph{cis} -stereoisomer (oleic acid) has been reported to be an inhibitor for the homolog OleT_{JE}. [30] Furthermore, by using high H₂O₂ concentrations, and taking

Table 2 Binding affinities (K_d) determined for the titration of fatty acids to H_2O_2 treated WT $OleT_{Sa}$. Thermodynamic parameters and the calculated K_{spin} for the spin state equilibrium as well as the percentage of high-spin species (HS) determined for the various $OleT_{Sa}$ samples.

	<i>K</i> _d (μΜ)	K _{spin} (20 °C)	ΔH (kcal/ mol)	ΔS (cal/ mol K)	ΔG (kcal/ mol)	% HS (20 °C)
OleT _{Sa} :	-	$\begin{array}{c} 1.07 \pm \\ 0.01 \end{array}$	$\begin{array}{c} \textbf{4.2} \pm \\ \textbf{0.1} \end{array}$	$14.5 \pm \\ 0.4$	-0.04 ± 0.003	43
OleT _{Sa} : $C_{20:0}$	$\begin{array}{c} 0.19 \\ \pm \ 0.04 \end{array}$	$\begin{array}{c} 2.38 \pm \\ 0.10 \end{array}$	$\begin{array}{c} 4.1 \; \pm \\ 0.3 \end{array}$	$15.5\ \pm$ 0.7	-0.51 ± 0.01	70
OleT _{Sa} : C _{18:0}	0.54 ± 0.02	$\begin{array}{c} 1.09 \pm \\ 0.2 \end{array}$	5.0 ± 0.3	17.3 ± 0.4	-0.05 ± 0.01	52
OleT _{Sa} : C _{18:1}	0.16 ± 0.03	-	-	-	-	42
OleT _{Sa} :	10.6 ± 0.50	$\begin{array}{c} 0.65 \pm \\ 0.01 \end{array}$	7.0 ± 0.3	$\begin{array}{c} \textbf{23.0} \pm \\ \textbf{0.9} \end{array}$	0.25 ± 0.005	40
$C_{12:0}$ Ole T_{Sa} : H_2O_2	± 0.50 -	$0.01 \\ 0.22 \pm \\ 0.005$	6.0 ± 0.6	17.5 ± 0.7	0.88 ± 0.01	18

^a As purified.

advantage of Compound II stability, we can use it as a backstop to reconstruct a Compound I absorption spectrum (Fig. 6D). The stopped-flow kinetic for the unsaturated and saturated C18 fatty acids are similar with slight variations in rate constants observed, but in overall good agreement with previously reported rate constants for $OleT_{JE}$ and $OleT_{Sa}$ with a protonated $C_{20:0}$ substrate $(k_1\sim 10^5\,M^{-1}\,s^{-1};\,k_2\,380-700\,s^{-1}$ and $k_3\,10-60\,s^{-1}).$ [20,24,30] Our data can be represented by the mechanism depicted in Fig. 7B, which despite not using perdeuterated substrates, all key intermediates can be detected and rate constants obtained.

The X-ray structure of as purified OleT_{Sa} revealed that the acid:base pair between the conserved I helix Arg243 and the carboxylate head group of the fatty acid, required to facilitate peroxygenase activity in CYP152s, had been displaced by an acetate ion, most likely due to its high concentrations in the crystallisation buffer. Inducing CYP152 members into being reactive on non-fatty acid substrates has been achieved using 'decoy' molecules. [54] The first-generation decoy molecules were short chained fatty acids that initiated the acid:base pair enabling peroxygenase activity to hydroxylate a small substrate that could still access the distal heme pocket. [54] Later work identified that a high concentration of acetate ions (1 M) could also instigate reactivity (hydroxylation) with non-fatty acid substrates, whilst retaining H₂O₂ as the co-substrate. [50] Therefore, the as purified $OleT_{Sa}$ X-ray structure serendipitously reveals how the most minimalistic of decoy molecules can initiate salt-bridge interactions with the I helix Arg side chain, and as a result, push a bound unsaturated fatty acid along the cavity

Much of the investigations into factors stabilising substrate binding and product outcomes of CYP152 decarboxylases has centred on the substrate cavity housing the alkyl chain. On the other hand, the importance of the I helix Arg in facilitating peroxygenase activity is well documented, to initiate the catalytic acid:base pair. Within the I helix of \mbox{OleT}_{Sa} , Asn243 (widely conserved across \mbox{OleT} members) would appear to serve as a H-bonding anchor point to orientate the Arg246 into a productive conformation to form the acid:base pair (Fig. 9B and C). Creation of the N243A variant reveals the Asn has a stabilising effect on the high-spin species and from metabolic profiling is required to obtain comparable levels of product conversion as observed for the WT. Thus H-bonding disruption to the I helix Arg clearly has effect and warrants further investigation amongst \mbox{OleT} members.

A general trend observed in $OleT_{Sa}$ is that binding of longer alkyl chains stabilise the formation of the high-spin heme form (Table 2). Indeed, the X-ray structure presented here reveals that $OleT_{Sa}$ would comfortably accommodate a C20 alkyl chain. Two structural motifs have been identified in CYP152s that help stabilise fatty acid binding which in

Table 3 EPR spectral simulation parameters for the simulations presented in Fig. 5A.

Sample	Component	g_1	g_2	g ₃	g_{av}	$gStrain_1$	$gStrain_2$	$gStrain_3$	%
As purified	1	2.53	2.25	1.88	2.22	0.099	0.033	0.047	57
	2	2.65	2.25	1.83	2.24	0.140	0.014	0.081	43
H_2O_2	1	2.48	2.24	1.90	2.21	0.076	0.022	0.030	33
	2	2.55	2.25	1.87	2.22	0.074	0.074	0.031	20
H_2O_2	3	2.62	2.26	1.84	2.24	0.115	0.014	0.050	20
	4	2.71	2.25	1.79	2.25	0.141	0.012	0.070	27
	1	2.49	2.24	1.89	2.21	0.075	0.025	0.033	22
0	2	2.54	2.24	1.87	2.22	0.060	0.056	0.034	20
C ₂₀	3	2.63	2.26	1.84	2.24	0.122	0.016	0.070	34
	4	2.71	2.25	1.79	2.25	0.157	0.012	0.068	24

Table 4 Binding affinities (K_d) determined for titration of fatty acids to H_2O_2 treated variants of $OleT_{Sa}$. Thermodynamic parameters and the calculated K_{spin} for the spin state equilibrium as well as the percentage of high-spin species (HS) determined for the various $OleT_{Sa}$ variant samples.

	<i>K</i> _d (μM)	K _{spin} (20 °C)	ΔH (kcal/ mol)	ΔS (cal/ mol K)	ΔG (kcal/ mol)	% HS (20 °C)
L39F:C _{20:0}	0.43 ±	$1.30 \pm$	3.3 \pm	11.7 \pm		57
	0.04	0.01	0.2	0.8	± 0.003	
L39F:C _{18:0}	0.34 \pm	-	-	-	-	-
	0.04					
L39F:C _{18:1}	$0.73 \pm$	-	-	-	-	-
	0.12					
L39F:C _{12:0}	12.35	-	-	-	_	-
	$\pm~0.72$					
L39F:H ₂ O ₂	-	0.31 \pm	7.2 \pm	22.4 \pm	0.68 \pm	25
		0.010	0.4	0.3	0.02	
L79T:C _{20:0}	0.10 \pm	-	-	-		-
	0.03					
L79T:C _{18:0}	$0.21~\pm$	_	_	_	-	-
	0.02					
F174A:	-	0.75 \pm	5.6 \pm	18.7 \pm	$0.16~\pm$	43
$C_{20:0}$		0.004	0.1	0.3	0.003	
F174A:	_	$0.23~\pm$	$9.7 \pm$	30.0 \pm	0.86 \pm	11
H_2O_2		0.011	1.2	2.4	0.029	
I177A: _{C20:0}	0.22 \pm	_	_	-	_	_
	0.07					
N243A:	0.15 \pm	0.34 \pm	6.8 \pm	21.0 \pm	$0.62\ \pm$	25
C _{20:0}	0.03	0.003	0.3	2.3	0.005	
N243A:	-	0.18 \pm	6.7 \pm	19.4 \pm	0.98 \pm	15
H_2O_2		0.004	0.5	1.4	0.011	

turn influences chemoselectivity and product rate conversions. [30,31,55] These are an extended F/G loop and a hydrophobic motif, known as the 'hydrophobic cradle', which lies some 15 Å away from the I helix Arg:carboxylate interaction site. [30,31,55]. OleT_{Sa} belongs to CYP152 members with an extended F/G loop, which shows high sequence similarity (77.8 %) with its close homolog $OleT_{JE}$ (inset Fig. 9A). Only two other X-ray structures of OleT members possessing an extended F/G loop have been reported. Alignment of the Ca carbons of $OleT_{Sa}$ with the $C_{20:0}$ bound $OleT_{JE}$ X-ray structure (PDB 4140) [21] gives a RMSD of 0.66 Å. For the OleT from L. alkaliphilus (PDB 9JQM) [49] a RMSD of 0.49 Å is determined, demonstrating high structural similarity amongst extended F/G loop members. Neither $OleT_{Sa}$ nor $OleT_{JE}$ possess a 'hydrophobic cradle' motif. Some OleT members have been reported to have the ability to decarboxylate unsaturated fatty acids. [30,31] These members have been shown to possess an extended 'hydrophobic cradle' and lack an extended F/G loop. An engineered extend F/G loop has been inserted into OleT_{RN}, which natively decarboxylates oleic acid (the cisisomer of elaidic acid), but the presence of the F/G loop becomes detrimental to product conversion. [30] For OleTsa, that has the extended F/G loop but lacks the 'hydrophobic cradle', product conversion to a diene is possible with a trans unsaturated fatty acid and based on the high structural similarity with other extended F/G loop CYP152s

such a conversion is also likely to be the case.

From the OleT_{Sa} X-ray structure the unsaturated substrate is displaced from its primary binding position i.e. Arg:carboxylate interaction and shifts along the cavity. It is notable that this movement induces no changes to side chain orientations within the cavity from comparison with the X-ray structure of OleT_{JE} with the longer C_{20:0} bound. [21] Thus, the displaced fatty acid fills the vacant space that is available to house longer alkyl chains e.g. C20, but is likely to remain stabilised owing to its proximity to the F/G loop and maintaining van der Waals contacts with Phe174 and Ile177. This suggests that for OleT members with extended F/G loops the cavity is rigid, compared to OleT members possessing a 'hydrophobic cradle' motif, where elements of plasticity (e. g. side chain rotations) have been reported that allows for the cavity to expand or contract depending on the alkyl chain length of the substrate. [31] Substituting substrate cavity residues that have van der Waals contacts with the bound fatty acid such as Phe174 or Ile177 results in the low- to high-spin heme transition being less favoured (Table 4), but less so for the adjacent Leu79. Even the L39F variant, located furthest from the heme and at the end of the cavity (Fig. 9) has a decreased K_{spin} value when bound to a C_{20:0} substrate (Table 4), indicative of Leu39 (or this remote region) having a contributing role in stabilising the high-spin state. Substituting Leu176 to a Gly in OleT_{JE} (equivalent to Ile177 in OleT_{Sa}), completely abolished the low- to high spin transition but substrate binding was confirmed and decarboxylase activity was greatly reduced in favour of product hydroxylation with stearic acid. [55] In the case of the OleT_{Sa} I177A variant, we find that although the low- to highspin transition is not observed on fatty acid binding, metabolic profiling with stearic and elaidic acids shows only decarboxylation. This could be a consequence of the methyl group of the Ala maintaining stearic control of the F/G loop to allow substrate orientation for decarboxylation as compared to the Gly substitution in OleT_{JE}. [55] Although the magnitude of the low- to high-spin spectral shifts are observed in both EPR and UV-vis spectroscopies differed depending on alkyl chain length and saturation as well mutation, this appears to have little effect on the metabolic activity of WT and variants with the C18 substrates.

5. Conclusions

Understanding the physicochemical properties, mechanism of action, and structural intricacies of CYP152 decarboxylases will help provide a blueprint for engineering this family of heme enzymes into robust biocatalysts for future implementation into biotechnology pipelines. In this respect our work has identified that a *trans*-stereoisomer of a monounsaturated fatty acid substrate can be accommodated and turned over in the binding cavity, therefore expanding the sustainable substrate space available to OleT members with an extended F/G loop. Furthermore, this work reinforces the view that substrate binding in decarboxylases involves a dynamic interplay of many factors that include alkyl chain length, interactions with the F/G loop and nearby residues, as well as H-bonding interactions within the I helix, although surprisingly these have minimal impact on chemoselectivity with the C18 fatty acids tested.

CRediT authorship contribution statement

Lewis J. Williams: Writing – review & editing, Writing – original draft, Methodology, Investigation, Formal analysis, Data curation, Conceptualization. Michael T. Wilson: Writing – review & editing, Methodology, Investigation, Formal analysis. James A. Birrell: Writing – review & editing, Methodology, Investigation, Formal analysis. Harry W. Lang: Investigation. Stephen G. Bell: Writing – review & editing, Methodology, Investigation, Formal analysis. Jonathan A.R. Worrall: Writing – review & editing, Writing – original draft, Supervision, Funding acquisition, Formal analysis, Data curation, Conceptualization.

Author statement

- The work described has not been published previously.
- The article is not under consideration for publication elsewhere.
- The article's publication is approved by all authors and tacitly or explicitly by the responsible authorities where the work was carried out
- If accepted, the article will not be published elsewhere in the same form, in English or in any other language, including electronically, without the written consent of the copyright-holder.

Declaration of competing interest

The authors declare that they have no known competing financial interests or personal relationships that could have appeared to influence the work reported in this paper.

Acknowledgements

LJW was supported by a joint studentship award (STU0436) from Diamond Light Source and the University of Essex. John Green is acknowledged for technical support with GC-MS. For the assistance with the construction of several site-directed variants, Luke Wheeler, Harry Youngman, Rabana Saith, Valeria Villa Velazquez Alfaro, and Theo Stavrinos are gratefully acknowledged. Access to the I04 beamline at Diamond Light Source was through the support of the East of England Macromolecular Crystallography BAG (mx32728).

Appendix A. Supplementary data

Supplementary data to this article can be found online at https://doi.org/10.1016/j.jinorgbio.2025.113117.

References

- [1] D.R. Nelson, Biochim. Biophys. Acta, Proteins Proteomics 1866 (2018) 141–154.
- [2] M.J. Coon, Annu. Rev. Pharmacol. Toxicol. 45 (2005) 1–25.
- [3] G. Di Nardo, G. Gilardi, Trends Biochem. Sci. 45 (2020) 511-525.
- [4] T.L. Poulos, Chem. Rev. 114 (2014) 3919-3962.
- [5] J.T. Groves, G.A. McClusky, J. Am. Chem. Soc. 98 (1976) 859–861.
- [6] X. Huang, J.T. Groves, J. Biol. Inorg. Chem. 22 (2017) 185–207.
- [7] D. Holtmann, F. Hollmann, Chembiochem 17 (2016) 1391–1398.
- [8] F. Hannemann, A. Bichet, K.M. Ewen, R. Bernhardt, Biochim. Biophys. Acta 1770 (2007) 30–344.
- [9] V.B. Urlacher, M. Girhard, Trends Biotechnol. 37 (2019) 882-897.
- [10] H. Joo, Z. Lin, F.H. Arnold, Nature 399 (1999) 670-673.
- [11] S. Fan, Z. Cong, Acc. Chem. Res. 57 (2024) 613-624.
- [12] M.N. Podgorski, J. Akter, L.R. Churchman, J.B. Bruning, J.J. De Voss, S.G. Bell, ACS Catal. 14 (2024) 7426–7443.
- [13] I. Matsunaga, A. Ueda, N. Fujiwara, T. Sumimoto, K. Ichihara, Lipids 34 (1999) 841–846.
- [14] I. Matsunaga, T. Sumimoto, A. Ueda, E. Kusunose, K. Ichihara, Lipids 35 (2000) 365–371.
- [15] M.A. Rude, T.S. Baron, S. Brubaker, M. Alibhai, S.B. Del Cardayre, A. Schirmer, Appl. Environ. Microbiol. 77 (2011) 1718–1727.
- [16] J.A. Amaya, C.D. Rutland, T.M. Makris, J. Inorg. Biochem. 158 (2016) 11-16.
- [17] H. Xu, L. Ning, W. Yang, B. Fang, C. Wang, Y. Wang, J. Xu, S. Collin, F. Laeuffer, L. Fourage, S. Li, Biotechnol. Biofuels 10 (2017) 208.
- [18] H.M. Girvan, H. Poddar, K.J. McLean, D.R. Nelson, K.A. Hollywood, C.W. Levy, D. Leys, A.W. Munro, J. Inorg. Biochem. 188 (2018) 18–28.

- [19] Y. Jiang, Z. Li, C. Wang, Y.J. Zhou, H. Xu, S. Li, Biotechnol. Biofuels 12 (2019) 79.
- [20] J.A. Amaya, O.M. Manley, J.C. Bian, C.D. Rutland, N. Leschinsky, S.C. Ratigan, T. M. Makris, J. Inorg. Biochem. 252 (2024) 112458.
- [21] J. Belcher, K.J. McLean, S. Matthews, L.S. Woodward, K. Fisher, S.E.J. Rigby, D. R. Nelson, D. Potts, M.T. Baynham, D.A. Parker, D. Leys, A.W. Munro, J. Biol. Chem. 289 (2014) 6535–6550.
- [22] S. Matthews, J.D. Belcher, K.L. Tee, H.M. Girvan, K.J. McLean, S.E. Rigby, C. W. Levy, D. Leys, D.A. Parker, R.T. Blankley, A.W. Munro, J. Biol. Chem. 292 (2017) 5128–5143.
- [23] J.L. Grant, C.H. Hsieh, T.M. Makris, J. Am. Chem. Soc. 137 (2015) 4940-4943.
- [24] J.L. Grant, M.E. Mitchell, T.M. Makris, Proc. Natl. Acad. Sci. USA 113 (2016) 10049–10054.
- [25] M.R. Sarkar, S.D. Houston, G.P. Savage, C.M. Williams, E.H. Krenske, S.G. Bell, J. J. De Voss, J. Am. Chem. Soc. 141 (2019) 19688–19699.
- [26] A.M. Kirk, J.E. Stok, S.H. Wong, T. Coleman, V.L. Challinor, J.N. Herring, J. B. Bruning, P.V. Bernhardt, S.G. Bell, E.H. Krenske, J.J. De Voss, ACS Catal. 15 (2025) 1274–1286
- [27] A.W. Munro, K.J. McLean, J.L. Grant, T.M. Makris, Biochem. Soc. Trans. 46 (2018) 183-106
- [28] D.S. Lee, A. Yamada, H. Sugimoto, I. Matsunaga, H. Ogura, K. Ichihara, S. Adachi, S.Y. Park, Y. Shiro, J. Biol. Chem. 278 (2003) 9761–9767.
- [29] T. Fujishiro, O. Shoji, S. Nagano, H. Sugimoto, Y. Shiro, Y. Watanabe, J. Biol. Chem. 286 (2011) 29941–29950.
- [30] L.L. Rade, W.C. Generoso, S. Das, A.S. Souza, R.L. Silveira, M.C. Avila, P.S. Vieira, R.Y. Miyamoto, A.B.B. Lima, J.A. Aricetti, R.R. de Melo, N. Milan, G.F. Persinoti, A. Bonomi, M.T. Murakami, T.M. Makris, L.M. Zanphorlin, Proc. Natl. Acad. Sci. USA 120 (2023) e2221483120.
- [31] W.C. Generoso, A.H.S. Alvarenga, I.T. Simões, R.Y. Miyamoto, R.R. Melo, E.P. X. Guilherme, F. Mandelli, C.A. Santos, R. Prata, C.R.D. Santos, F.M. Colombari, M. A.B. Morais, R. Pimentel Fernandes, G.F. Persinoti, M.T. Murakami, L. M. Zanphorlin, Nat. Commun. 16 (2025) 945.
- [32] L. Zhang, D. Ma, Y. Yin, Q. Wang, Chemistry 27 (2021) 8940–8945.
- [33] I.M. Monirul, H.H. Masjuki, M.A. Kalam, N.W.M. Zulkifli, H.K. Rashedul, M. M. Rashed, H.K. Imdadul, M.H. Mosarof, RSC Adv. 5 (2015) 86631–86655.
- [34] E. Gasteiger, A. Gattiker, C. Hoogland, I. Ivanyi, R.D. Appel, A. Bairoch, Nucleic Acids Res. 31 (2003) 3784–3788.
- [35] J.F. Morrison, Biochim. Biophys. Acta Enzymol. 185 (1969) 269-286.
- [36] S. Stoll, A. Schweiger, J. Magn. Reson. 178 (2006) 42–55.
- [37] M.T. Wilson, J. Torres, Stopped-flow spectroscopy, in: M.G. Gore (Ed.), Spectrophotometry and Spectrofluorimetry: A Practical Approach 225, OUP, 2000, pp. 209–239.
- [38] R.J. Gildea, J. Beilsten-Edmands, D. Axford, S. Horrell, P. Aller, J. Sandy, J. Sanchez-Weatherby, C.D. Owen, P. Lukacik, C. Strain-Damerell, R.L. Owen, M. A. Walsh, G. Winter, Acta Crystallogr. Sect. D 78 (2022) 752–769.
- [39] J. Agirre, M. Atanasova, H. Bagdonas, C.B. Ballard, A. Basle, J. Beilsten-Edmands, R.J. Borges, D.G. Brown, J.J. Burgos-Marmol, J.M. Berrisford, P.S. Bond, I. Caballero, L. Catapano, G. Chojnowski, A.G. Cook, K.D. Cowtan, T.I. Croll, J. E. Debreczeni, N.E. Devenish, E.J. Dodson, T.R. Drevon, P. Emsley, G. Evans, P. R. Evans, M. Fando, J. Foadi, L. Fuentes-Montero, E.F. Garman, M. Gerstel, R. J. Gildea, K. Hatti, M.L. Hekkelman, P. Heuser, S.W. Hoh, M.A. Hough, H. T. Jenkins, E. Jimenez, R.P. Joosten, R.M. Keegan, N. Keep, E.B. Krissinel, P. Kolenko, O. Kovalevskiy, V.S. Lamzin, D.M. Lawson, A.A. Lebedev, A.G. W. Leslie, B. Lohkamp, F. Long, M. Maly, A.J. McCoy, S.J. McNicholas, A. Medina, C. Millan, J.W. Murray, G.N. Murshudov, R.A. Nicholls, M.E.M. Noble, R. Oeffner, N.S. Pannu, J.M. Parkhurst, N. Pearce, J. Pereira, A. Perrakis, H.R. Powell, R. J. Read, D.J. Rigden, W. Rochira, M. Sammito, F. Sanchez Rodriguez, G. M. Sheldrick, K.L. Shelley, F. Simkovic, A.J. Simpkin, P. Skubak, E. Sobolev, R. A. Steiner, K. Stevenson, I. Tews, J.M.H. Thomas, A. Thorn, J.T. Valls, V. Uski, I. Uson, A. Vagin, S. Velankar, M. Vollmar, H. Walden, D. Waterman, K.S. Wilson, M.D. Winn, G. Winter, M. Wojdyr, K. Yamashita, Acta Crystallogr. Sect. D 79 (2023) 449-461.
- [40] R.M. Keegan, M.D. Winn, Acta Crystallogr. Sect. D 64 (2008) 119-124.
- [41] K. Cowtan, Acta Crystallogr. Sect. D 62 (2006) 1002–1011.
- [42] G.N. Murshudov, A.A. Vagin, E.J. Dodson, Acta Crystallogr. Sect. D 53 (1997)
- [43] P. Emsley, B. Lohkamp, W.G. Scott, K. Cowtan, Acta Crystallogr. Sect. D 66 (2010) 486–501.
- [44] F. Long, R.A. Nicholls, P. Emsley, S. Graéeulis, A. Merkys, A. Vaitkus, G. N. Murshudov, Acta Crystallogr. Sect. D 73 (2017) 112–122.
- [45] S.G. Sligar, Biochemistry 15 (1976) 5399-5406.
- [46] J.S. Harbort, J.J. De Voss, J.E. Stok, S.G. Bell, J.R. Harmer, in: G. Hanson, L. Berliner (Eds.), Future Directions in Metalloprotein and Metalloenzyme Research, Springer International Publishing, Cham, 2017, pp. 103–142.
- [47] A. Midlik, V. Navrátilová, T.R. Moturu, J. Koča, R. Svobodová, K. Berka, Sci. Rep. 11 (2021) 12345.
- [48] D. Leys, C.G. Mowat, K.J. McLean, A. Richmond, S.K. Chapman, M.D. Walkinshaw, A.W. Munro, J. Biol. Chem. 278 (2003) 5141–5147.
- [49] S. Phaisan, A. Phintha, D. Trisrivirat, N. Lawan, J. Sucharitakul, A. Charoenpol, P. Watthaisong, H. Tanaka, G. Kurisu, P. Chaiyen, J. Biol. Chem. 301 (2025) 110397.
- [50] H. Onoda, O. Shoji, Y. Watanabe, Dalton Trans. 44 (2015) 15316-15323.
- [51] C.M. Krest, E.L. Onderko, T.H. Yosca, J.C. Calixto, R.F. Karp, J. Livada, J. Rittle, M. T. Green, J. Biol. Chem. 288 (2013) 17074–17081.
- [52] Y. Li, S. Wu, L. Wang, Y. Li, F. Shi, X. Wang, J. Sci. Food Agric. 90 (2010) 1380–1383.

- [53] L.-H. Wang, X.-A. Zeng, M.-S. Wang, C.S. Brennan, D. Gong, Biochim. Biophys. Acta Biomembr. 1860 (2018) 481–490.
 [54] O. Shoji, T. Fujishiro, H. Nakajima, M. Kim, S. Nagano, Y. Shiro, Y. Watanabe, Angew. Chem. Int. Ed. 46 (2007) 3656–3659.
- [55] J.A. Amaya, C.D. Rutland, N. Leschinsky, T.M. Makris, Biochemistry 57 (2018) 344–353.